

# Space-time boundary elements on graded meshes for 3D elastodynamics

Alessandra Aimi<sup>+</sup>, Luca Desiderio<sup>§</sup>, Heiko Gimperlein<sup>§\*</sup>, Chiara Guardasoni<sup>++</sup>

<sup>+</sup>*Department of Mathematical, Physical and Computer Sciences,  
University of Parma, Parma, Italy.*

<sup>§</sup>*Department of Mathematics and Computer Sciences, Physical Sciences and Earth Sciences,  
University of Messina, Messina, Italy.*

<sup>§</sup>*Engineering Mathematics, University of Innsbruck, Innsbruck, Austria.*

## Abstract

The solution to the elastodynamic equations in the exterior of a polygonal or polyhedral domain or a screen exhibits singularities at corners and edges. This paper presents a space-time boundary element method in 3D on algebraically graded meshes to resolve these singularities, based on recently obtained error estimates for the weakly singular integral equation. Numerical examples show the efficiency of the proposed approach. They confirm the theoretically predicted, quasi-optimal convergence rates and study the singular behavior of the solution for typical 3D geometries with edges, corners or cone points.

*Keywords:* 3D elastodynamics; space-time boundary elements; geometric singularities; graded meshes

## 1 Introduction

The displacement and stress of an elastic body exhibit singular behavior from edges, corners or cone points. Their asymptotic behavior near such geometric singularities is well-understood for static problems [17, 25, 29]. Numerically, singular expansions of the displacement and stresses are the basis of efficient approximations by  $h$ ,  $p$  and  $hp$  finite [37] or boundary element methods [27], which recover the optimal convergence rates known for smooth solutions.

Corresponding methods for elastodynamic problems are only starting to be explored. Foundational works by Plamenevskiĭ and collaborators [31, 30] demonstrate that the transient displacement and stresses exhibit singular behavior of the same kind as in static problems. More precisely, their results imply that at any given time the transient singular expansions near an edge or a cone point involve the same singular functions known from the static case, with coefficients varying smoothly in time. Müller and Schwab [32] later used these analytical results to obtain optimal convergence rates for a finite element method on graded meshes in 2D polygonal domains. Recent work by Aimi, Di Credico, Gimperlein and Stephan [4] extends the theoretical analysis to  $h$  and  $hp$  boundary element methods for elastodynamics, confirmed by numerical experiments in 2D model cases.

In this article we study  $h$ -versions of the boundary element method for elastodynamics in 3D polyhedral domains or, as the most challenging case, in the complement of a polygonal screen. The singular expansion of the boundary traction leads to quasi-optimal convergence rates for boundary

---

\*Corresponding Author, Heiko.Gimperlein@uibk.ac.at

<sup>†</sup>A. Aimi, L. Desiderio and C. Guardasoni are members of the INdAM-GNCS Research Group, Italy. L. Desiderio is a member of the Accademia Peloritana dei Pericolanti, Messina, Italy.

element approximations on algebraically graded meshes. Detailed numerical experiments confirm the predicted convergence rates and the precise singular behavior of the solutions.

To be specific, we consider elastodynamic wave propagation in a polyhedral domain or outside a polygonal screen, with prescribed displacement on the boundary  $\Gamma$ . To solve this problem numerically, we formulate it as an equivalent time-dependent integral equation for the single layer operator on the boundary. Its solution is numerically approximated using a space-time Galerkin boundary element method based on tensor product elements on a quasi-uniform or graded mesh for  $\Gamma$  in space and a uniform mesh in time.

As obtained in [4], the approximation rate is governed by the above-mentioned geometric singularities of the traction on the boundary. We review the behavior of traction and displacement for typical singular 3D geometries and, in a Theorem in Subsection 5.2, deduce an a priori error estimate for the error of the  $h$ -method on algebraically graded meshes. Essentially, the convergence rate on  $\beta$ -graded meshes (defined in Subsection 5.1) is improved by a factor  $\beta$  with respect to the rate on quasi-uniform meshes, until the quasi-optimal rate  $\frac{3}{2}$  is achieved for large  $\beta$ . Note that, unlike in two space dimensions, quasi-optimal convergence rates cannot be obtained on shape-regular meshes: the thin, anisotropic elements of a graded mesh are required for the quasi-optimal approximation of edge singularities.

Detailed numerical experiments are presented in typical 3D geometries with edges, corners or cone points. They study the convergence rates on algebraically graded and quasi-uniform meshes for these singular geometries, as well as the leading singular behavior of the solution. The numerical results underline the theoretical predictions.

Our work contributes to the active developments in boundary element methods for acoustic and elastodynamic wave equations based on both space-time Galerkin and convolution quadrature methods, see [8, 16, 28, 21] for an overview. Our approach is based on formulations related to the energy of the system [1], which assures unconditional stability. The application of boundary element methods to problems in elastodynamics has a long history in engineering [5], and the mathematical analysis was started in [10, 11] for scattering and for crack problems. Recent works on the numerical analysis and computational aspects of elastodynamic problems include [3, 4, 13, 18, 20, 36].

For time independent elastic problems in polygonal or polyhedral domains, the study of singular expansions near non-smooth boundary points has a long history, partly motivated by the difficulty to compute quantities of interest like stress intensity factors. Beyond the general references mentioned at the beginning of this Introduction, we refer to [6, 7, 9, 12, 15, 34] for examples and applications motivating the current work. Based on such expansions, von Petersdorff [35] first derived quasi-optimal convergence rates for boundary elements on algebraically graded meshes for the Laplace equation.

*The article is organized as follows:* after presenting the model problem in the Section 2, Section 3 reviews the singular expansion of displacement and stress near non-smooth boundary points, like edges, corners and cone points. The weak formulation of the boundary integral equation is discussed in Section 4. Section 5 then introduces the boundary element discretization based on piece-wise polynomial approximations of the solution for uniform time steps and algebraically graded meshes in space. It presents an a priori error estimate, showing a quasi-optimal convergence rate, and discusses the algorithmic realization of the proposed approach. Detailed numerical results are the content of Section 6. Section 7 outlines our conclusions. The relevant definitions of function spaces and norms that are used in the analysis are recalled in an Appendix.

## 2 Model problem

In the Euclidean space  $\mathbb{R}^3$  equipped with a fixed orthonormal Cartesian coordinate system  $\mathbf{x} = (x_1, x_2, x_3)^\top$  with origin at  $\mathbf{O} = (0, 0, 0)^\top$ , we consider a screen or a closed surface  $\Gamma$  and its connected exterior, denoted by  $\Omega$ . Further, let  $J := [0, T]$  be a time interval for a given final time instant  $T > 0$ . Under the assumptions of small displacement theory and in absence of external

sources, elastodynamic wave propagation is described by the following boundary value problem for the Navier-Cauchy equation of motion:

$$\begin{cases} \varrho \ddot{\mathbf{u}}(\mathbf{x}; t) - \nabla \cdot \boldsymbol{\sigma}[\mathbf{u}](\mathbf{x}; t) = \mathbf{0} & (\mathbf{x}; t) \in \Omega \times J & (2.1a) \\ \mathbf{u}(\mathbf{x}; t) = \bar{\mathbf{u}}(\mathbf{x}; t) & (\mathbf{x}; t) \in \Gamma \times J & (2.1b) \\ \mathbf{u}(\mathbf{x}; 0) = \mathbf{0} & \mathbf{x} \in \Omega & (2.1c) \\ \dot{\mathbf{u}}(\mathbf{x}; 0) = \mathbf{0} & \mathbf{x} \in \Omega, & (2.1d) \end{cases}$$

where  $\mathbf{u}(\mathbf{x}; t) = (u_1, u_2, u_3)^\top(\mathbf{x}; t)$  and  $\boldsymbol{\sigma}[\mathbf{u}](\mathbf{x}; t)$  represent, respectively, the unknown displacement field and the stress tensor at point  $\mathbf{x}$  and time  $t$ . In addition,  $\varrho$  is the mass density of the medium occupying  $\Omega$ . In problem (2.1), homogeneous initial conditions are assumed at the first time of interest  $t = 0$  and a Dirichlet type boundary condition  $\bar{\mathbf{u}}(\mathbf{x}; t) = (\bar{u}_1, \bar{u}_2, \bar{u}_3)^\top(\mathbf{x}; t)$  is prescribed on  $\Gamma$ . Furthermore, the superposed dot indicates time differentiation, while  $\nabla$  denotes the nabla operator. According to linear elasticity theory, the stress-strain relation allows us to express the tensor  $\boldsymbol{\sigma}[\mathbf{u}]$  as follows:

$$\boldsymbol{\sigma}[\mathbf{u}](\mathbf{x}; t) := \lambda [\nabla \cdot \mathbf{u}(\mathbf{x}; t)] \mathbf{I} + \mu [\nabla \mathbf{u}(\mathbf{x}; t) + \nabla \mathbf{u}^\top(\mathbf{x}; t)], \quad (2.2)$$

$\mathbf{I}$  being the 3-by-3 identity tensor, while  $\mu$  and  $\lambda$  being the shear modulus and the Lamé parameter, respectively. Since we can separate equation (2.1a) into solutions for the pressure wave (P-wave in short) and the shear wave (S-wave in short) by taking the divergence and curl respectively, the elastic parameters  $\mu$  and  $\lambda$  are related to the primary and secondary wave speeds  $c_p^2 := (\lambda + 2\mu)\varrho^{-1}$  and  $c_s^2 := \mu\varrho^{-1}$ .

A crucial property of the Navier-Cauchy equation is the energy balance. For all  $t \in J$  the time-dependent energy functional is defined as the sum of the kinetic energy and the total strain energy [33], i.e.:

$$E(t) := \frac{1}{2} \left\{ \int_{\Omega} \dot{\mathbf{u}}^2(\mathbf{x}; t) d\mathbf{x} + c_s^2 \int_{\Omega} \nabla \mathbf{u}(\mathbf{x}; t) : \nabla \mathbf{u}(\mathbf{x}; t) d\mathbf{x} + (c_p^2 - c_s^2) \int_{\Omega} [\nabla \cdot \mathbf{u}(\mathbf{x}; t)]^2 d\mathbf{x} \right\}, \quad (2.3)$$

where the symbol  $:$  stands for the double inner tensor product. Testing (2.1a) against  $\dot{\mathbf{u}}(\mathbf{x}; t)$ , integrating over  $\Omega$  and using Green's formula implies that

$$\frac{d}{dt} E(t) = \int_{\Gamma} \mathbf{p}(\mathbf{u})^\top(\mathbf{x}; t) \dot{\mathbf{u}}(\mathbf{x}; t) d\Gamma_{\mathbf{x}} \quad (2.4)$$

where  $\mathbf{p}(\mathbf{u})(\mathbf{x}; t)$  stands for the traction vector  $\boldsymbol{\sigma}[\mathbf{u}](\mathbf{x}; t) \cdot \mathbf{n}_{\mathbf{x}}$  (in case of a screen, if  $\Gamma^-$  and  $\Gamma^+$  denote respectively the lower and the upper face of  $\Gamma$ , then  $\mathbf{n}_{\mathbf{x}}$  is oriented from  $\Gamma^-$  to  $\Gamma^+$ ). Integrating the relationship (2.4) over  $J$ , the homogeneous initial conditions allow us to derive the following energy balance equation:

$$E(T) = \int_0^T \int_{\Gamma} \mathbf{p}(\mathbf{u})^\top(\mathbf{x}; t) \dot{\mathbf{u}}(\mathbf{x}; t) d\Gamma_{\mathbf{x}} dt. \quad (2.5)$$

To solve (2.1) numerically, we formulate it as an equivalent time dependent integral equation on  $\Gamma \times J$ , as briefly recalled in the following Section 4, i.e. we study

$$\mathbf{V}[\mathbf{w}](\mathbf{x}; t) = \left( \mathbf{K} + \frac{1}{2} \mathbf{I} \right) [\bar{\mathbf{u}}](\mathbf{x}; t), \quad (\mathbf{x}, t) \in \Gamma \times J, \quad (2.6)$$

where  $\mathbf{w} := \mathbf{p}(\mathbf{u})|_{\Gamma \times J}$ , involving the weakly singular integral operator  $\mathbf{V}$  and, on the right-hand side the double layer integral operator  $\mathbf{K}$ , defined from a fundamental solution  $\mathbf{G}$  to (2.1a) and

its traction  $\mathbf{p}_y(\mathbf{G})$ , respectively, as

$$\begin{aligned}\mathbf{V}[\boldsymbol{\Phi}](\mathbf{x}; t) &= \int_0^t \int_{\Gamma} \mathbf{G}(\mathbf{x}, \mathbf{y}; t, \tau) \boldsymbol{\Phi}(\mathbf{y}; \tau) d\Gamma_{\mathbf{y}} d\tau, \\ \mathbf{K}[\boldsymbol{\Psi}](\mathbf{x}; t) &= \int_0^t \int_{\Gamma} \mathbf{p}_y(\mathbf{G})(\mathbf{x}, \mathbf{y}; t, \tau)^T \boldsymbol{\Psi}(\mathbf{y}, \tau) d\Gamma_{\mathbf{y}} d\tau.\end{aligned}$$

Kernel tensor  $\mathbf{G}$  represents the response of the elastic medium to a unidirectional unit  $\delta$ -Dirac impulse in space and time. In particular, its entries:

$$\begin{aligned}G_{ij}(\mathbf{x}, \mathbf{y}; t, \tau) &:= \frac{1}{4\pi\varrho c_p^2} \frac{r_i r_j}{r^3} \delta\left(t - \tau - \frac{r}{c_p}\right) + \frac{1}{4\pi\varrho c_s^2} \left(\frac{\delta_{ij}}{r} - \frac{r_i r_j}{r^3}\right) \delta\left(t - \tau - \frac{r}{c_s}\right) + \\ &\quad - \frac{1}{4\pi\varrho} \left(\frac{\delta_{ij}}{r^3} - \frac{r_i r_j}{r^5}\right) (t - \tau) \left[ H\left(t - \tau - \frac{r}{c_p}\right) - H\left(t - \tau - \frac{r}{c_s}\right) \right],\end{aligned}\tag{2.7}$$

provide the  $i$ -th component of the displacement at the observation point  $\mathbf{x}$  and observation time  $t$ , due to a force in the  $j$ -th direction at the source point  $\mathbf{y}$  and emission time  $\tau$ . Moreover, they depend only on the difference  $\mathbf{r} := \mathbf{x} - \mathbf{y}$  and  $t - \tau$ , but not on the source point  $\mathbf{y}$  and the emission time  $\tau$  themselves. Note that in (2.7)  $H(\cdot)$  is the Heaviside function, while  $\delta(\cdot)$  is the Dirac impulse.

### 3 Singular expansion near non-smooth boundary points

For the time independent Lamé equations of elastostatics in a singular domain, detailed asymptotic expansions of the solution at non-smooth boundary points have been studied extensively, partly motivated by applications to computing quantities of interest like stress intensity factors, see e.g. [12, 15, 24, 25, 34]. We describe key results for the elastodynamic equations in geometries with edges, cone points or corners, as relevant to this article. There the solution admits a singular expansion into a leading part of explicit singular functions plus smoother remainder terms.

#### 3.1 2d sector / polygon

- *Elastostatic equation*

We first review the time independent Lamé equations in the simple case of a polygon or sector  $\Omega \subset \mathbb{R}^2$ . There the singular functions at a vertex  $V_j$  are explicitly given in polar coordinates  $(r, \phi)$  centered at  $V_j$ , depending on the opening angle  $\omega_j$  at the vertex and the elastic parameters. The result is the basis to describe edge singularities of domains in  $\mathbb{R}^3$  and for the corresponding elastodynamic problems.

**Proposition 3.1.** *Near a vertex  $V_j$ , with interior opening angle  $\omega_j$ , the solution  $\mathbf{u} \in H^1(\Omega)^2$  of the time independent Lamé equations with sufficiently regular Dirichlet boundary data admits the decomposition*

$$\mathbf{u}(r, \phi) = \mathbf{u}_{0,j}(r, \phi) + \sum_k a_{jk}^* \mathbf{S}_{jk}^*(r, \phi) \chi_j(r)\tag{3.1}$$

with a regular part  $\mathbf{u}_0 \in H^{1+s}(\Omega)^2$ ,  $s > 0$  depending on the boundary data,  $a_{jk}^* \in \mathbb{C}$ , the singular functions

$$\mathbf{S}_{jk}^*(r, \phi) = \begin{cases} r^{\nu_{jk}^*} \boldsymbol{\varphi}_{jk}^*(\phi), & \text{for } \nu_{jk}^* \notin \mathbb{N}, \\ r^{\nu_{jk}^*} \ln r \boldsymbol{\varphi}_{jk}^*(\phi) + r^{\nu_{jk}^*} \tilde{\boldsymbol{\varphi}}_{jk}^*(\phi), & \text{for } \nu_{jk}^* \in \mathbb{N} \end{cases}\tag{3.2}$$

with  $\boldsymbol{\varphi}_{jk}^*, \tilde{\boldsymbol{\varphi}}_{jk}^*$  defined below, and  $\chi_j$  smooth cut-off functions localized at  $V_j$ . The singular exponents  $\nu_{jk}^* \in \mathbb{C}$  with  $\text{Re } \nu_{jk}^* > 0$  are solutions of the equations

$$\sin \nu_{jk}^* \omega_j = \pm \frac{\nu_{jk}^*}{k^*} \sin \omega_j,\tag{3.3}$$

where  $k^* = 3 - 4\nu$  and  $\nu := \frac{\lambda}{2\lambda + \mu}$  is the Poisson ratio. The functions  $\varphi_{jk}^*$  with the components  $(\varphi_{jk}^*)_r$  in  $r$ -direction and  $(\varphi_{jk}^*)_\phi$  in  $\phi$ -direction are of the form

$$(\varphi_{jk}^*)_r = A \cos(1 + \nu_{jk}^*)\phi + B \sin(1 + \nu_{jk}^*)\phi + C \cos(1 - \nu_{jk}^*)\phi + D \sin(1 - \nu_{jk}^*)\phi \quad (3.4)$$

$$(\varphi_{jk}^*)_\phi = -A \sin(1 + \nu_{jk}^*)\phi + B \cos(1 + \nu_{jk}^*)\phi - \gamma_{jk} C \sin(1 - \nu_{jk}^*)\phi + \gamma_{jk} D \cos(1 - \nu_{jk}^*)\phi \quad (3.5)$$

with constants  $A, B, C, D \in \mathbb{C}$  depending on the material parameters and  $\gamma_{jk} = \frac{3 + \nu_{jk}^* - 4\nu}{3 - \nu_{jk}^* - 4\nu}$ . The functions  $\tilde{\varphi}_{jk}^*$  are a linear combination of  $\cos((1 \pm \nu_{jk}^*)\phi)$ ,  $\phi \cos((1 \pm \nu_{jk}^*)\phi)$ ,  $\sin((1 \pm \nu_{jk}^*)\phi)$  and  $\phi \sin((1 \pm \nu_{jk}^*)\phi)$ .

- *Elastodynamic equation*

The singular behavior of the solution to the elastodynamic equations is then studied using a Fourier transform in time [31, 4, 32]. In particular, Corollary 3.6 in [4] finds that in a neighborhood of  $V_j$  the solution to the elastodynamic equations admits the expansion

$$\mathbf{u}(r, \phi, t) = \mathbf{u}_0(r, \phi, t) + \sum_k (X c_{jk}^*)(r, \phi, t) \mathbf{S}_{jk}^*(r, \phi), \quad (3.6)$$

for suitable  $c_{jk}^*$  involving the same singular functions  $\mathbf{S}_{jk}^*$  and singular exponents  $\nu_{jk}^*$  as the time independent problem. The smoothing operator  $X$  is here given by

$$Xc(r, \phi, t) = \mathcal{F}_{\tau \rightarrow t}^{-1} (\chi(|\tau|r \cos \phi, |\tau|r \sin \phi) \hat{c}(\tau)),$$

with a suitable cut-off function  $\chi$ .

- *Laplace and scalar wave equations*

We also require a corresponding description of the singularities for the scalar wave equation

$$\rho \partial_t^2 u - \Delta u = 0,$$

with Dirichlet boundary conditions imposed near a vertex  $V_j$  of  $\Omega$ . For the time independent problem

$$-\Delta u = 0,$$

near  $V_j$  the solution  $u$  admits the decomposition

$$u(r, \phi) = u_0(r, \phi) + \sum_k a_{jk} S_{jk}(r, \phi) \chi_j(r) \quad (3.7)$$

analogous to Proposition 3.1, with the singular functions now given by

$$S_{jk}(r, \phi) = \begin{cases} r^{\nu_{jk}} \varphi_{jk}(\phi), & \text{for } \nu_{jk} \notin \mathbb{N}, \\ r^{\nu_{jk}} \ln r \varphi_{jk}(\phi) + r^{\nu_{jk}} \tilde{\varphi}_{jk}(\phi), & \text{for } \nu_{jk} \in \mathbb{N}. \end{cases} \quad (3.8)$$

The singular exponents are explicitly computable as  $\nu_{jk} = \frac{k\pi}{\omega_j}$ ,  $\varphi_{jk}(\phi) = \sin(\nu_{jk}\phi)$  and  $\tilde{\varphi}_{jk}(\phi) = \cos(\nu_{jk}\phi)$ ,  $k \in \mathbb{N}$ .

The singular expansion (3.7) for the time independent problem translates into an expansion for the time dependent problem, analogous to (3.6), but with the singular functions  $S_{jk}$  replacing  $\mathbf{S}_{jk}^*$  and suitable coefficients  $c_{jk}$  replacing  $c_{jk}^*$ .

### 3.2 3d wedge

The behavior of solutions in a wedge of opening angle  $\omega$ , denoted by  $\Omega = \mathbb{K} \times \mathbb{R}$  with  $\mathbb{K} = \{(r, \phi) : r > 0, \phi \in (0, \omega)\}$ , generalizes the discussion in Section 3.1 from dimension  $n = 2$  to  $n = 3$ . As an example, the wedge  $\mathbb{K} \times \mathbb{R}$  is a model for the curved edge between the base and the lateral surface of the cone illustrated in Figure 1. We omit the index  $j$  in the discussion for polygons, as long as we consider the model geometry with only one non-smooth subset  $\{\mathbf{0}\} \times \mathbb{R}$  of  $\partial\Omega$ . For the time dependent problem the singular expansion of the solution near the edge  $\{\mathbf{0}\} \times \mathbb{R}$  is given by, in cylindrical coordinates and denoting by  $x_3$  the coordinate along the edge of the wedge:

$$\begin{aligned} \mathbf{u}(r, \phi, x_3, t) = & \mathbf{u}_0(r, \phi, x_3, t) + \sum_{k, \ell} (Xc_{k\ell})(r, \phi, x_3, t) \mathbf{S}_{k\ell}(r, \phi) \\ & + \sum_{k, \ell} (Xc_{k\ell}^*)(r, \phi, x_3, t) \mathbf{S}_{k\ell}^*(r, \phi). \end{aligned} \quad (3.9)$$

Here, the singular functions  $\mathbf{S}_{k\ell}$  and  $\mathbf{S}_{k\ell}^*$  are constructed from those in Section 3.1 ((3.8), respectively (3.2)). The smoothing operator  $X$  for the edge is given by

$$Xc(r, \phi, x_3, t) = \mathcal{F}_{(\xi, \tau) \rightarrow (x_3, t)}^{-1} \left( \chi(\sqrt{|\xi|^2 + |\tau|^2})(r \cos \phi, r \sin \phi) \hat{c}(\xi, \tau) \right)$$

for  $\hat{c} = \hat{c}_{k\ell}, \hat{c}_{k\ell}^*$ . We refer to Section 3.2 in [4] and to [31] for a detailed analysis.

By considering the coordinate  $x_3$  along the edge as a parameter, the expansion recovers those for polygonal domains in  $\mathbb{R}^2$  in Section 3.1.

Applications to boundary integral equations require the Neumann trace of the solution  $\mathbf{u}$  of the inhomogeneous Dirichlet problem and the given initial conditions. As in (3.9), we obtain the leading singular behavior

$$\mathbf{w}(r, \phi, x_3, t) = \mathbf{b}(\phi, x_3, t) r^{\nu^* - 1} + \mathbf{w}_0(r, \phi, x_3, t). \quad (3.10)$$

Here,  $\nu^*$  denotes the leading singular exponent,  $\mathbf{b}$  is smooth for smooth data and  $\mathbf{w}_0$  is a less singular remainder.

### 3.3 3d cone

We now consider the elastodynamic equations in the exterior of an infinitely extended cone  $\mathbb{K}$  with vertex at  $r = 0$  and opening angle  $\Theta$ . The model geometry of a finitely extended cone of opening angle  $\Theta$  is illustrated at the top of Figure 1. The singular behavior of solutions to the elastostatic Lamé equations has been studied, in particular, in [9, 12], in dependence on  $\Theta$  and the elastic parameters.

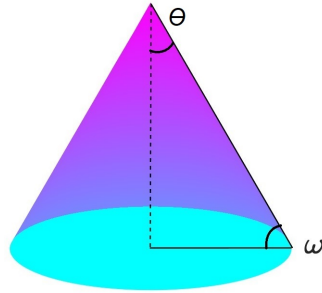


Figure 1: Model geometry of a 3d cone with opening angle  $\Theta$ . This includes also a curved wedge, between the lateral surface and the basis, of opening angle  $\omega$ .

Using spherical coordinates  $(r, \phi, \theta)$ , local orthonormal basis vectors are given by

$$\begin{aligned}\mathbf{e}_r &= (\sin(\theta) \cos(\phi), \sin(\theta) \sin(\phi), \cos(\theta))^\top, \\ \mathbf{e}_\theta &= (\cos(\theta) \cos(\phi), \cos(\theta) \sin(\phi), -\sin(\theta))^\top, \\ \mathbf{e}_\phi &= (-\sin(\phi), \cos(\phi), 0)^\top.\end{aligned}$$

We write the components of a vector  $\mathbf{u}$  in this basis as  $\mathbf{u} = u_r \mathbf{e}_r + u_\theta \mathbf{e}_\theta + u_\phi \mathbf{e}_\phi$ . For the time independent problem Beagles and Sändig [12] use Papkovitch-Neuber potentials to construct the general form of rotationally symmetric solutions from the ansatz

$$\mathbf{u} = 4(1 - \nu) \mathbf{B} - \nabla(\mathbf{x} \cdot \mathbf{B} + B_4) \quad (3.11)$$

with Poisson's ratio  $\nu$  and where the components of  $\mathbf{B} = (B_1, B_2, B_3)^\top$  and  $B_4$  are harmonic functions. In spherical coordinates the ansatz (3.11) is written as

$$\begin{aligned}\mathbf{u} &= (u_r, u_\theta, u_\phi)^\top = (3 - 4\nu)(\mathbf{B} \cdot \mathbf{e}_r, \mathbf{B} \cdot \mathbf{e}_\theta, \mathbf{B} \cdot \mathbf{e}_\phi)^\top \\ &\quad - (r \mathbf{e}_r \cdot \partial_r \mathbf{B} + \partial_r B_4, \mathbf{e}_r \cdot \partial_\theta \mathbf{B} + \frac{1}{r} \partial_\theta B_4, \frac{1}{\sin(\theta)} \mathbf{e}_r \cdot \partial_\phi \mathbf{B} + \frac{1}{r \sin(\theta)} \partial_\phi B_4)^\top.\end{aligned} \quad (3.12)$$

To find the rotationally symmetric solutions (which also describe the generic leading behavior), we set  $B_1 = B_2 = 0$ ,

$$B_3 = c_1 r^\alpha P_\alpha(\cos(\theta)), \quad B_4 = c_2 r^{\alpha+1} P_{\alpha+1}(\cos(\theta)),$$

where  $P_\alpha(\cos(\theta))$  are Legendre functions of the first kind and the singular exponent  $\alpha > 0$  together with the coefficients  $c_1, c_2$  are obtained below. Substitution into (3.12) gives the singular functions for the cone

$$\mathbf{u}(r, \theta) = c_1 r^\alpha \begin{pmatrix} A_{11}(\alpha, \theta) \\ A_{21}(\alpha, \theta) \end{pmatrix} + c_2 r^\alpha \begin{pmatrix} B_{11}(\alpha, \theta) \\ B_{21}(\alpha, \theta) \end{pmatrix} \quad (3.13)$$

with

$$(A_{11}(\alpha, \theta), A_{21}(\alpha, \theta)) = ((3 - 4\nu - \alpha) P_\alpha(\cos(\theta)), P'_\alpha(\cos(\theta)) \cos(\theta) \sin(\theta) - (3 - 4\nu) P_\alpha(\cos(\theta)) \sin(\theta)),$$

as well as  $(B_{11}(\alpha, \theta), B_{21}(\alpha, \theta)) = (-(\alpha + 1) P_{\alpha+1}(\cos(\theta)), \sin(\theta) P'_{\alpha+1}(\cos(\theta)))$ . The singular exponents  $\alpha$  are computed as the roots of the equation

$$\det \begin{pmatrix} A_{11}(\alpha, \theta) & B_{11}(\alpha, \theta) \\ A_{21}(\alpha, \theta) & B_{21}(\alpha, \theta) \end{pmatrix} = 0.$$

Substituting for  $A_{11}, A_{21}, B_{11}, B_{21}$ , this equation for  $\alpha$  takes the following form:

$$\begin{aligned}0 &= \frac{-(\alpha + 1)}{\sin(\theta)} (P_\alpha^2(\cos(\theta)) \cos(\theta) (\alpha + 4\nu - 3) \\ &\quad + P_\alpha(\cos(\theta)) P_{\alpha+1}(\cos(\theta)) (3 - 4\nu - \cos^2(\theta) (2\alpha + 1)) + P_{\alpha+1}^2(\cos(\theta)) \cos(\theta) (\alpha + 1)) .\end{aligned} \quad (3.14)$$

Imposing homogeneous Dirichlet conditions on  $\mathbf{u}$  in (3.13) determines the coefficients  $c_1, c_2$  and hence the corresponding eigenfunction. We refer to [12] for numerical results for the zeros  $\alpha$  and their dependence on the opening angle  $\theta$  and Poisson's ratio  $\nu$ .

For the time independent problem, the singular expansion of the solution near the cone tip is based on the singular functions from (3.13) and the exponents  $\alpha$  which are the roots in (3.14), and it can be expressed as

$$\mathbf{u}(r, \phi, \theta) = \sum_{k, \ell} \tilde{a}_\ell^k(\phi) \mathbf{u}_\ell^k(r, \theta) + \mathbf{u}_0(r, \phi, \theta). \quad (3.15)$$

The singular expansion translates into a singular expansion for the time dependent problem, see Section 3.3 in [4]:

$$\mathbf{u}(r, \phi, \theta, t) = \sum_{k, \ell} \tilde{c}_\ell^k(r, \phi, \theta, t) \mathbf{u}_\ell^k(r, \theta) + \mathbf{u}_0(r, \phi, \theta, t). \quad (3.16)$$

For applications to boundary integral equations we again require the Neumann trace at  $\theta = \Theta$  of the solution  $\mathbf{u}$  of the inhomogeneous Dirichlet problem with given initial conditions. For the cone we obtain the leading singular behavior

$$\mathbf{w}(r, \phi, t) = \chi(r) r^{\alpha-1} \mathbf{b}(\phi, t) + \mathbf{w}_0(r, \phi, t), \quad (3.17)$$

for the leading root  $\alpha$  of (3.14) and a suitable cut-off function  $\chi$  localized in a neighborhood of the cone tip,  $r = 0$ . Here,  $\mathbf{b}$  is smooth for smooth data and  $\mathbf{w}_0$  a less singular remainder.

For both the wedge and the cone, we may assume, after possibly expanding  $\mathbf{w}_0$  further in (3.10), respectively (3.17), that the regular part  $\mathbf{w}_0$  is sufficiently smooth in space. Corresponding expansions then also hold for the solutions  $\mathbf{w}$  to the integral equation, see also (4.2).

### 3.4 Polygonal screens and polyhedral domains in 3d

Beyond the geometries considered in Sections 3.1-3.3, singularities at corner points are of significant interest. The simplest case is given by a flat polygonal screen  $\Gamma \subset \mathbb{R}^3$ , where singularities arise from the edges and corner points. For time independent problems in this geometry, asymptotic expansions and their implications for the numerical approximation are discussed, for example, in [17, 35]. For the time dependent scalar wave equation, see [22, 23].

We describe the decomposition of the solution and its traction on  $\Gamma$  near a vertex in terms of polar coordinates  $(r, \theta)$  centered at this point. Approaching the screen from the upper, respectively lower sides of the screen, we obtain the boundary values  $\mathbf{u}_\pm$ , which now involve vertex, singular and regular edge-vertex, as well as edge singularities.

$$\begin{aligned} \mathbf{u}(t, r, \theta)|_\pm &= C(t) \chi(r) r^\lambda \Phi(\theta) + C_1(t) \tilde{\chi}(\theta) \beta_1(r) (\sin(\theta))^{\frac{1}{2}} \\ &\quad + C_2(t) \tilde{\chi}(\frac{\pi}{2} - \theta) \beta_2(r) (\cos(\theta))^{\frac{1}{2}} + \mathbf{u}_0(t, r, \theta) \\ &=: \mathbf{u}^v + \mathbf{u}_1^{ev} + \mathbf{u}_2^{ev} + \mathbf{u}_0. \end{aligned} \quad (3.18)$$

The corresponding decomposition of the traction is given by

$$\begin{aligned} \mathbf{p}(t, r, \theta)|_\pm &= C'(t) \chi(r) r^{\lambda-1} \Phi'(\theta) + C'_1(t) \tilde{\chi}(\theta) \beta'_1(r) r^{-1} (\sin(\theta))^{-\frac{1}{2}} \\ &\quad + C'_2(t) \tilde{\chi}(\frac{\pi}{2} - \theta) \beta'_2(r) r^{-1} (\cos(\theta))^{-\frac{1}{2}} + \mathbf{w}_0(t, r, \theta) \\ &=: \mathbf{w}^v + \mathbf{w}_1^{ev} + \mathbf{w}_2^{ev} + \mathbf{w}_0. \end{aligned} \quad (3.19)$$

Here  $\beta_j(r)$  behaves like  $r^{\lambda-\frac{1}{2}}$  near  $r = 0$ , while  $\beta'_j(r)$  behaves like  $r^\lambda$ ,  $j = 1, 2$ . Compared to the local coordinates near the edge in the previous section, the polar angle  $\theta$  corresponds to the distance to the edge and the radius  $r$  to the variable  $x_3$  along the edge.

For a rectangular screen  $\Gamma = (0, 1) \times (0, 1) \times \{0\}$ , the corner exponent  $\lambda \simeq 0.2966$ . The behavior of the corner exponent  $\lambda$  for a flat polygonal screen is analyzed in [40]: it is independent of material parameters, and the singularity becomes monotonically weaker, varying from  $r^{-1}$  to  $r^0$ , as the angle of the corner varies from  $2\pi$  to 0.

Expansions for polyhedral domains similarly involve edge, vertex and edge-vertex singularities. The leading singular behavior near an edge coincides with that from Section 3.2. The leading singular behavior at a corner is studied, for example, in [6, 7]. The singular exponent  $\lambda$  is obtained as the lowest eigenvalue of a spectral problem for an elliptic operator on a spherical polygonal domain with Dirichlet boundary conditions. It generally has to be computed numerically, and we refer to [6, 7] for efficient methods.



## 4 Energetic time-domain BIE weak formulation

The basic machinery for deriving a BIE formulation of equation (2.1a) is a classical one and can be found in any textbook on PDEs and boundary integral equations (see for example [14] and [26]). Hence, starting from the well known integral representation formula of the solution  $\mathbf{u}(\mathbf{x}; t)$  to (2.1a)

$$\mathbf{u}(\mathbf{x}; t) = \mathbf{V}[\mathbf{p}(\mathbf{u})](\mathbf{x}; t) - \mathbf{K}[\mathbf{u}](\mathbf{x}; t), \quad (\mathbf{x}, t) \in \Omega \times J, \quad (4.1)$$

when  $\mathbf{x}$  approaches the boundary  $\Gamma$ ,  $\mathbf{u}$  tends to  $\bar{\mathbf{u}}$  according to the Dirichlet boundary condition in (2.1b). Consequently, with the help of a limiting process, we obtain the formulation of the elastodynamic problem as the integral equation (2.6) of the first kind on  $\Gamma \times J$ . Setting  $\mathbf{g} := (\mathbf{K} + \frac{1}{2}\mathbf{I})[\bar{\mathbf{u}}]$ , we write this equation in the form

$$\mathbf{V}[\mathbf{w}](\mathbf{x}; t) = \mathbf{g}(\mathbf{x}; t), \quad (\mathbf{x}, t) \in \Gamma \times J. \quad (4.2)$$

Using the solution  $\mathbf{w}$  from (4.2) and the Dirichlet datum, the representation formula (4.1) allows to evaluate the solution  $\mathbf{u}(\mathbf{x}; t)$  to the elastodynamic problem in every point of  $\Omega \times J$ .

For the numerical solution with a Galerkin boundary element method, we need to write (4.2) in a weak form involving suitable space-time Sobolev spaces and related norms, which are shortly recalled in the Appendix. For the interested reader, more details can be found in [19]. Having introduced the space-time bilinear form

$$\mathcal{B}_E(\mathbf{w}, \mathbf{v}) = \int_0^T \int_{\Gamma} \mathbf{v}^\top(\mathbf{x}; t) \frac{\partial}{\partial t} \mathbf{V}[\mathbf{w}](\mathbf{x}; t) d\Gamma_{\mathbf{x}} dt, \quad (4.3)$$

the weak formulation of (4.2) consists in finding  $\mathbf{w} \in H_\sigma^0(\mathbb{R}^+; \tilde{H}^{-1/2}(\Gamma))^3$  such that:

$$\mathcal{B}_E(\mathbf{w}, \mathbf{v}) = \int_0^T \int_{\Gamma} \mathbf{v}^\top(\mathbf{x}; t) \dot{\mathbf{g}}(\mathbf{x}; t) d\Gamma_{\mathbf{x}} dt \quad \forall \mathbf{v} \in H_\sigma^0(\mathbb{R}^+; \tilde{H}^{-1/2}(\Gamma))^3. \quad (4.4)$$

As discussed in [3],  $\mathcal{B}_E$  is continuous and (weakly) coercive in the sense that

$$\|\mathbf{w}\|_{0, -\frac{1}{2}, \Gamma, *}^2 \leq \mathcal{B}_E(\mathbf{w}, \mathbf{w}) \leq \|\mathbf{w}\|_{1, -\frac{1}{2}, \Gamma, *}^2. \quad (4.5)$$

The weak boundary integral equation (4.4) for the Dirichlet problem is well-posed, due to (4.5).

Note that while the theoretical analysis requires  $\sigma > 0$  on the unbounded time interval  $\mathbb{R}^+$ , it is common in practical computations to use  $\sigma = 0$  [38].

The weak formulation (4.4) is often called energetic because it relates to the elastodynamic energy. Namely, if we choose the test function  $\mathbf{v} = \mathbf{w}$ , the energy balance (2.5) allows us to obtain the identity:

$$\mathcal{B}_E(\mathbf{w}, \mathbf{w}) = \int_0^T \int_{\Gamma} \mathbf{w}^\top(\mathbf{x}; t) \dot{\mathbf{g}}(\mathbf{x}; t) d\Gamma_{\mathbf{x}} dt = \frac{1}{2} E(T) + \int_0^T \int_{\Gamma} \mathbf{w}^\top(\mathbf{x}; t) \frac{\partial}{\partial t} \mathbf{K}[\bar{\mathbf{u}}](\mathbf{x}; t) d\Gamma_{\mathbf{x}} dt. \quad (4.6)$$

The bilinear form  $\mathcal{B}_E(\mathbf{w}, \mathbf{w})$  on the left-hand side therefore agrees with a multiple of the energy  $E(T)$ , up to a term which involves the Dirichlet datum.

## 5 Approximation by space-time BEM

In order to numerically approximate the solution of the weak formulation (4.4), we introduce a space-time boundary element method. In the following we describe the Galerkin discretization of (4.4) on  $\beta$ -graded meshes, use the singular expansions from Section (3) to obtain quasi-optimal convergence rates and describe the algorithmic details of the proposed approach.

## 5.1 Discretization

We restrict our attention to tensor product space-time discretisations of  $\Sigma := \Gamma \times J$ . To be specific, for the time discretization we consider a decomposition  $\mathcal{T}_{\Delta_t}(J)$  of the time interval  $J$  into subintervals  $J_n := [t_n, t_{n+1}]$  with constant time step  $\Delta_t := T/N_{\Delta_t}$ , such that  $t_n := n\Delta_t$  for  $n = 0, \dots, N_{\Delta_t}$ .

In space we consider the approximation on quasiuniform and graded meshes  $\mathcal{T}_{\Delta_x}(\Gamma) = \bigcup_{j=1}^{M_{\Delta_x}} E_j$ , consisting of triangles  $E_j, j = 1, \dots, M_{\Delta_x}$ . We denote by  $\Delta_x$  the longest side of a triangle.

To define a  $\beta$ -graded mesh on the interval  $[-1, 1]$ , for parameter  $\beta > 0$ , by symmetry it suffices to specify the nodes in  $[-1, 0]$ . There we let

$$x_k = -1 + \left(\frac{k}{N_l}\right)^\beta \quad (5.1)$$

for  $k = 1, \dots, N_l$ . On the square  $[-1, 1]^2$ , the nodes of a  $\beta$ -graded mesh are given by tuples of such points,  $(x_k, x_l)$ ,  $k, l = 1, \dots, N_l$ , see Figure 2.

We refer to Section 6 for illustrations of graded meshes on more general polyhedral geometries, which are locally modeled on the previous examples. In all cases, a quasiuniform mesh is recovered for  $\beta = 1$ .

Associated to the triangulation  $\mathcal{T}_{\Delta_x}(\Gamma)$ , we choose a basis  $\{\varphi_m\}_{m=1}^{M_{\Delta_x}}$  of Lagrangian shape functions for the space  $X_{\Delta_x}^0$  of piecewise constant polynomials. Similarly, for the time discretization, we fix a basis  $\{\bar{\varphi}_n\}_{n=0}^{N_{\Delta_t}-1}$  of shape functions, for the space  $X_{\Delta_t}^0$  of piecewise constant polynomials associated to  $\mathcal{T}_{\Delta_t}(J)$ . Note that, in what follows, we assume:

$$\bar{\varphi}_n(t) := H(t - t_n) - H(t - t_{n+1}) \quad \text{for } n = 0, \dots, N_{\Delta_t}.$$

We define the space-time mesh  $\mathcal{T}_{\Delta_x, \Delta_t}(\Sigma) := \mathcal{T}_{\Delta_t}(J) \times \mathcal{T}_{\Delta_x}(\Gamma)$ . The corresponding approximation spaces are given as a tensor product of  $X_{\Delta_t}^0$  and  $X_{\Delta_x}^0$ . We set  $\mathbf{X}_{\Delta_x, \Delta_t}^{0,0} := (X_{\Delta_t}^0 \otimes X_{\Delta_x}^0)^3$ .

Finally, to discretise the variational formulation (4.4), we replace the unknown density field  $\mathbf{w} \in H_\sigma^0(\mathbb{R}^+; H^{-1/2}(\Gamma))^3$  and the test function  $\mathbf{v} \in H_\sigma^0(\mathbb{R}^+; H^{-1/2}(\Gamma))^3$  with their discrete counterparts in  $\mathbf{X}_{\Delta_x, \Delta_t}^{0,0}$ , respectively.

Consequently, we consider the problem of finding  $\mathbf{w}_{\Delta_x, \Delta_t} \in \mathbf{X}_{\Delta_x, \Delta_t}^{0,0}$  such that:

$$\mathcal{B}_E(\mathbf{w}_{\Delta_x, \Delta_t}, \mathbf{v}_{\Delta_x, \Delta_t}) = \int_0^T \int_\Gamma \mathbf{v}_{\Delta_x, \Delta_t}^\top(\mathbf{x}; t) \dot{\mathbf{g}}(\mathbf{x}; t) d\Gamma_x dt \quad \forall \mathbf{v}_{\Delta_x, \Delta_t} \in \mathbf{X}_{\Delta_x, \Delta_t}^{0,0}. \quad (5.2)$$

From the solution  $\mathbf{w}_{\Delta_x, \Delta_t}$  and the Dirichlet datum, the numerical approximations  $\mathbf{u}_{\Delta_x, \Delta_t}$  to the solution of the elastodynamic problem (2.1) is obtained in  $\Omega \times J$  using (4.1).

## 5.2 Convergence rates

The asymptotic expansion of the solution  $\mathbf{u}$  and, more specifically, the traction  $\mathbf{p}(\mathbf{u})$  on  $\Sigma$ , give rise to quasi-optimal convergence rates for the numerical solution of the discrete weak formulation (5.2) on graded meshes.

For a domain in  $\mathbb{R}^3$  with both wedge and cone singularities, the convergence rate will be determined by

$$\tilde{\alpha} = \min \left\{ \operatorname{Re} \nu^*, \operatorname{Re} \alpha + \frac{1}{2} \right\}, \quad (5.3)$$

which depends on the geometry and the elastic parameters. Here, we recall that  $\nu^*$  denotes the leading singular exponent at the edge (the minimum of  $\frac{\pi}{\omega}$  and the minimal root of (3.3)), while  $\alpha$  is the leading singular exponent at the cone tip (the leading zero of (3.14)). For a domain with only conical singularities, we set  $\tilde{\alpha} = \operatorname{Re} \alpha + \frac{1}{2}$ , while for a wedge domain in  $\mathbb{R}^3$ , we set  $\tilde{\alpha} = \operatorname{Re} \nu^*$ .

The most singular case is given by a screen in  $\mathbb{R}^3$ , respectively a crack in  $\mathbb{R}^2$ , where in both cases  $\nu^* = \frac{1}{2}$  is independent of the elastic parameters.

From [4] we recall quasi-optimal a-priori error estimates on graded meshes in these geometries:

**Theorem.** Let  $\varepsilon > 0$  and  $\sigma > 0$ . Let  $\mathbf{w} \in H_\sigma^r(\mathbb{R}^+; H^{-1/2}(\Gamma))^3$  be the solution to the single layer integral equation (2.6) and  $\mathbf{w}_{\Delta_x, \Delta_t} \in \mathbf{X}_{\Delta_x, \Delta_t}^{0,0}$  the best approximation to  $\mathbf{w}$  in the norm of  $H_\sigma^r(\mathbb{R}^+; H^{-1/2}(\Gamma))^3$  on a  $\beta$ -graded spatial mesh with  $\Delta t \lesssim \Delta_x$ . Then

$$\|\mathbf{w} - \mathbf{w}_{\Delta_x, \Delta_t}\|_{0, -\frac{1}{2}, \Gamma, *} \leq C_{\beta, \varepsilon} \Delta_x^{\min\{\beta\tilde{\alpha} - \varepsilon, \frac{3}{2}\}}, \quad (5.4)$$

where  $C_{\beta, \varepsilon}$  is a suitable constant depending on  $\beta$ ,  $\varepsilon$  and  $\mathbf{w}$ .

In particular, for  $\beta > \frac{3}{2\tilde{\alpha}}$  the convergence rate  $\frac{3}{2} - \varepsilon$  gets arbitrarily close to the rate  $\frac{3}{2}$  known for smooth geometries.

Corresponding convergence rates in the presence of corner singularities, as in Section 3.4, are determined by

$$\tilde{\alpha} = \min \left\{ \operatorname{Re} \nu^*, \operatorname{Re} \lambda + \frac{1}{2} \right\},$$

with the corner exponent  $\lambda$ . We refer to [22] for a discussion in the case of the time-dependent scalar wave equation, which is readily adapted to elastodynamics.

### 5.3 Algorithmic realization

Since the unknown discrete density field  $\mathbf{w}_{\Delta_x, \Delta_t}$  admits the representation

$$\mathbf{w}_{\Delta_x, \Delta_t}(\mathbf{x}; t) := \sum_{n=0}^{N_{\Delta_t}-1} \bar{\varphi}_n(t) \sum_{m=1}^{M_{\Delta_x}} \mathbf{w}_m^{(n)} \varphi_m(\mathbf{x}), \quad \mathbf{w}_m^{(n)} := \left( w_{m,1}^{(n)}, w_{m,2}^{(n)}, w_{m,3}^{(n)} \right)^\top$$

by testing equation (5.2) with basis functions, we obtain

$$\sum_{n=0}^{N_{\Delta_t}-1} \sum_{m=1}^{M_{\Delta_x}} \mathcal{B}_E(\varphi_m, \bar{\varphi}_n, \varphi_{\tilde{m}}, \bar{\varphi}_{\tilde{n}}) \mathbf{w}_m^{(n)} = \mathbf{g}_{\tilde{m}}^{(\tilde{n})} \quad \text{for } \tilde{m} = 1, \dots, M_{\Delta_x}, \tilde{n} = 1, \dots, N_{\Delta_t}$$

where

$$\mathcal{B}_E(\varphi_m, \bar{\varphi}_n, \varphi_{\tilde{m}}, \bar{\varphi}_{\tilde{n}}) = - \int_0^T \int_\Gamma \left( \int_0^t \int_\Gamma \mathbf{G}(\mathbf{x}, \mathbf{y}; t, \tau) \varphi_m(\mathbf{y}) \bar{\varphi}_n(\tau) d\Gamma_{\mathbf{y}} d\tau \right) \varphi_{\tilde{m}}(\mathbf{x}) \dot{\bar{\varphi}}_{\tilde{n}}(t) d\Gamma_{\mathbf{x}} dt$$

and

$$\mathbf{g}_{\tilde{m}}^{(\tilde{n})} = - \int_0^T \int_\Gamma \mathbf{g}(\mathbf{x}; t) \varphi_{\tilde{m}}(\mathbf{x}) \dot{\bar{\varphi}}_{\tilde{n}}(t) d\Gamma_{\mathbf{x}} dt.$$

We focus our attention on  $\mathcal{B}_E(\varphi_m, \bar{\varphi}_n, \varphi_{\tilde{m}}, \bar{\varphi}_{\tilde{n}})$ . As the fundamental solution depends only on the difference  $t - \tau$  and the considered decomposition of the time interval is uniform, the temporal integrals depend only on the difference  $\Delta_{\tilde{n}, n} := t_{\tilde{n}} - t_n$  and in particular they vanish if  $t_{\tilde{n}} < t_n$ . Thus, the duality pairing with all the basis functions leads to the block lower triangular Toeplitz system

$$\begin{pmatrix} \mathbf{E}^{(0)} & 0 & 0 & 0 & 0 \\ \mathbf{E}^{(1)} & \mathbf{E}^{(0)} & 0 & 0 & 0 \\ \mathbf{E}^{(2)} & \mathbf{E}^{(1)} & \mathbf{E}^{(0)} & 0 & 0 \\ \vdots & \vdots & \vdots & \ddots & \vdots \\ \mathbf{E}^{(N_{\Delta_t}-1)} & \mathbf{E}^{(N_{\Delta_t}-2)} & \mathbf{E}^{(N_{\Delta_t}-3)} & \dots & \mathbf{E}^{(0)} \end{pmatrix} \begin{pmatrix} \mathbf{w}^{(1)} \\ \mathbf{w}^{(2)} \\ \mathbf{w}^{(3)} \\ \vdots \\ \mathbf{w}^{(N_{\Delta_t}-1)} \end{pmatrix} = \begin{pmatrix} \mathbf{g}^{(1)} \\ \mathbf{g}^{(2)} \\ \mathbf{g}^{(3)} \\ \vdots \\ \mathbf{g}^{(N_{\Delta_t}-1)} \end{pmatrix} \quad (5.5)$$

where, for each  $\ell = \tilde{n} - n = 0, \dots, N_{\Delta_t} - 1$ , the block  $\mathbf{E}^{(\ell)}$  is a  $3M_{\Delta_x}$ -by- $3M_{\Delta_x}$  matrix, because each pair of spatial indices  $\tilde{m}, m = 1, \dots, M_{\Delta_x}$  does not define a single entry but rather a 3-by-3 subblock, i.e.

$$\left(\mathbf{E}_{\tilde{m},m}^{(\ell)}\right)_{ij} = - \int_0^T \int_{\Gamma} \left( \int_0^t \int_{\Gamma} G_{ij}(\mathbf{x}, \mathbf{y}; t, \tau) \varphi_m(\mathbf{y}) \bar{\varphi}_n(\tau) d\Gamma_{\mathbf{y}} d\tau \right) \varphi_{\tilde{m}}(\mathbf{x}) \dot{\bar{\varphi}}_{\tilde{n}}(t) d\Gamma_{\mathbf{x}} dt \quad (5.6)$$

A main challenge of the energetic BEM is the accurate and efficient evaluation of the quadruple integrals in (5.6). After a double analytic integration in the time variables, we obtain:

$$\left(\mathbf{E}_{\tilde{m},m}^{(\ell)}\right)_{ij} = -\frac{1}{4\pi\varrho} \sum_{\eta, \tilde{\eta}=0}^1 (-1)^{\eta+\tilde{\eta}} \int_{\Gamma} \int_{\Gamma} \mathbb{G}_{ij}(\mathbf{x}, \mathbf{y}; \Delta_{\tilde{n}+\tilde{\eta}, n+\eta}) \varphi_m(\mathbf{y}) \varphi_{\tilde{m}}(\mathbf{x}) d\Gamma_{\mathbf{y}} d\Gamma_{\mathbf{x}}. \quad (5.7)$$

where the components of the time-integrated kernel  $\mathbb{G}$  are given by

$$\begin{aligned} \mathbb{G}_{ij}(\mathbf{x}, \mathbf{y}; \Delta_{\tilde{n}, n}) &= \frac{1}{c_P^2} \frac{r_i r_j}{r^3} H\left(\Delta_{\tilde{n}, n} - \frac{r}{c_P}\right) + \frac{1}{c_S^2} \left(\frac{\delta_{ij}}{r} - \frac{r_i r_j}{r^3}\right) H\left(\Delta_{\tilde{n}, n} - \frac{r}{c_S}\right) + \\ &\quad - \frac{1}{2} \left(\frac{\delta_{ij}}{r^3} - \frac{r_i r_j}{r^5}\right) \left[ \left(\Delta_{\tilde{n}, n}^2 - \frac{r^2}{c_P^2}\right) H\left(\Delta_{\tilde{n}, n} - \frac{r}{c_P}\right) - \left(\Delta_{\tilde{n}, n}^2 - \frac{r^2}{c_S^2}\right) H\left(\Delta_{\tilde{n}, n} - \frac{r}{c_S}\right) \right] \end{aligned} \quad (5.8)$$

In the above relationship, the Heaviside functions represent the wave front propagation and their contribution is 0 or 1. If  $r < c_S \Delta_{\tilde{n}, n} < c_P \Delta_{\tilde{n}, n}$ , then (5.8) reduces to

$$\mathbb{G}_{ij}(\mathbf{x}, \mathbf{y}; \Delta_{\tilde{n}, n}) = \frac{1}{2} \left( \frac{r_i r_j}{r^3} \frac{c_P^2 - c_S^2}{c_P^2 c_S^2} + \frac{\delta_{ij}}{r} \frac{c_P^2 + c_S^2}{c_P^2 c_S^2} \right) \quad (5.9)$$

and we observe a space singularity of type  $\mathcal{O}(1/r)$  as  $r \rightarrow 0$ , which is typical of weakly singular kernels related to 3D elliptic problems. Moreover, when  $0 < c_S \Delta_{\tilde{n}, n} < r < c_P \Delta_{\tilde{n}, n}$ , (5.8) is no longer singular and becomes

$$\mathbb{G}_{ij}(\mathbf{x}, \mathbf{y}; \Delta_{\tilde{n}, n}) = \frac{1}{2} \left( \frac{1}{c_P^2} \frac{\delta_{ij}}{r} - \frac{1}{c_P^2} \frac{r_i r_j}{r^3} - \frac{\delta_{ij}}{r^3} \Delta_{\tilde{n}, n}^2 + 3 \frac{r_i r_j}{r^5} \Delta_{\tilde{n}, n}^2 \right). \quad (5.10)$$

For what concerns the double integration in space variables, we remember that we are considering lagrangian piecewise constant basis and test functions. Consequently, we can reduce the integrals over  $\Gamma$  to double integrals over the source and the field triangles  $E_{\tilde{m}}$  and  $E_m$  respectively. Thus, we consider

$$\left(\mathbf{E}_{\tilde{m},m}^{(\ell)}\right)_{ij} = -\frac{1}{4\pi\varrho} \sum_{\eta, \tilde{\eta}=0}^1 (-1)^{\eta+\tilde{\eta}} \int_{E_{\tilde{m}}} \int_{E_m} \mathbb{G}_{ij}(\mathbf{x}, \mathbf{y}; \Delta_{\tilde{n}+\tilde{\eta}, n+\eta}) d\Gamma_{\mathbf{y}} d\Gamma_{\mathbf{x}} \quad (5.11)$$

and we carry out the outer integration on the source triangle by applying a  $M_g$ -point suitable quadrature rule, so that

$$\left(\mathbf{E}_{\tilde{m},m}^{(\ell)}\right)_{ij} \simeq -\frac{1}{4\pi\varrho} \sum_{\eta, \tilde{\eta}=0}^1 (-1)^{\eta+\tilde{\eta}} \sum_{q=1}^{M_g} \omega_q \int_{E_m} \mathbb{G}_{ij}(\mathbf{x}_q, \mathbf{y}; \Delta_{\tilde{n}+\tilde{\eta}, n+\eta}) d\Gamma_{\mathbf{y}}, \quad (5.12)$$

where  $\mathbf{x}_q$  and  $\omega_q$  are the quadrature nodes and weights, respectively. The remaining integral requires integration over geometrically complicated intersections of the field triangle with two spherical surfaces of radii  $r_P = c_P \Delta_{\tilde{n}, n}$  and  $r_S = c_S \Delta_{\tilde{n}, n}$ , representing the wave fronts of the P- and S-waves. To address this issue, we project the source point  $\mathbf{x}_q$  onto the field triangle plane and we use a careful decomposition of the area of integration into sample standard shapes in polar

coordinates. Thus, the integration is performed analytically, as described in [3].

Finally, the space-time system (5.5) may be solved by a block forward substitution, that leads to a marching-on-in-time time stepping scheme, which is unconditionally stable and first-order accurate in  $\Delta_t$ . This is proved for scalar problems in [2] in the more general framework of an energetic BEM-FEM coupling. Therefore, under the assumption that the matrix  $\mathbf{E}^{(0)}$  is non singular, which is confirmed by all the numerical testing that has been performed on the energetic approach, at every time instant  $t_\ell$  with  $\ell = 0, \dots, N_{\Delta_t} - 1$ , one has to solve the reduced linear system

$$\mathbf{E}^{(0)} \mathbf{w}^{(\ell)} = \mathbf{g}^{(\ell)} - \sum_{k=0}^{\ell-1} \mathbf{E}^{(\ell-k)} \mathbf{w}^{(k)}.$$

We remark that blocks  $\mathbf{E}^{(\ell)}$ , with  $\ell = 1, \dots, N_{\Delta_t} - 1$ , are only used to update at every time step the right-hand side. For this reason the LU factorization on the block  $\mathbf{E}^{(0)}$  needs to be performed and stored only once at the beginning of the time stepping scheme.

## 6 Numerical results

In this section we present numerical experiments which validate the convergence properties of the proposed approach and study the singular behavior of the solution. We first discuss computational aspects common to all the experiments.

For the numerical evaluation of integrals that define the entries  $\mathbf{E}_{\tilde{m},m}^{(\ell)}$  in (5.12), we have applied a quadrature rule with  $M_g$  nodes and weights, obtained with the algorithm described in [39]. The choices  $M_g = 7$  for the first three examples,  $M_g = 12$  for the fourth example and  $M_g = 19$  for the last example have guaranteed the computation of the mentioned integrals with a sufficiently high accuracy. This is a key issue to assure the convergence and space-time accuracy of the energetic BEM in the context of 3D elastodynamic problems, whose theoretical analysis been performed in [4].

All the numerical computations have been performed on a cluster with two Intel<sup>®</sup> XEON<sup>®</sup> E5-2683v4 CPUs (2.1 GHz clock frequency and 16 cores) by means of parallel MATLAB<sup>®</sup> codes.

A natural measure of the error relies on the (squared) energy, which is defined from the identity (4.6) and computed in the discrete framework from the matrix  $\mathbf{E}$  or the right hand side vector  $\mathbf{g}$  and the solution vector  $\mathbf{w}$  as

$$\mathcal{E}(\mathbf{w}) := \mathbf{w}^\top \mathbf{E} \mathbf{w} = \mathbf{w}^\top \mathbf{g}. \quad (6.1)$$

We compute the squared energy error with respect to an extrapolated benchmark energy  $\mathcal{E}_\infty$  as

$$\text{Err}_L := \mathcal{E}_\infty - \mathcal{E}(\mathbf{w}_L) \quad (6.2)$$

where the subscript  $L$  refers to the refinement level.

In the first two examples, we study the numerical solution of the integral equation (4.2) on a flat screen  $\Gamma$  using the Galerkin formulation (5.2). The Dirichlet datum  $\mathbf{g}(\mathbf{x}; t) = (0, 0, x_1^2 \sin^5 t)^\top$ . The final time is set as  $T = 1$ , while the material parameters  $\varrho = 1$ ,  $\mu = 0.25$  and  $\lambda = 0.5$  are taken in such a way that  $c_p = 1$ ,  $c_s = 0.5$ , unless otherwise stated.

On the screen  $\Gamma$  we introduce an algebraically graded mesh, whose construction on a general polyhedral surface is described in [35]. In what follows,  $\beta \geq 1$  is the grading parameter of the mesh, and the level  $L \geq 1$  relates to the (square root of the) number of triangles on  $\Gamma$ . To study the convergence, we start by choosing a coarse mesh associated to the value  $L = 2$  and successively double the value of  $L$ .

**Example 1. Square screen.** We consider  $\Gamma := [-\ell, \ell]^2 \times \{x_3 = 0\}$ , with  $\ell = 0.5$ . Due to its symmetry with respect to the origin, the  $\beta$ -graded space mesh is generated on the bottom-left quarter of  $\Gamma$  by the nodes  $(x_{1,k}^{(L)}, x_{2,k}^{(L)})$ , where

$$x_{1,k}^{(L)} = \ell \left( -1 + \left( \frac{k}{L} \right)^\beta \right) \quad \text{and} \quad x_{2,h}^{(L)} = \ell \left( -1 + \left( \frac{h}{L} \right)^\beta \right), \quad \text{for } k, h = 0, \dots, L,$$

which have been then reflected to obtain a mesh on the whole screen. The total number of triangles is proportional to  $L^2$ .

Note that the parameter  $\Delta_{\mathbf{x}}$  is proportional to  $\ell_{\max} := \ell[1 - (1 - 1/L)^\beta]$ , while the parameter  $\ell_{\min} := \ell L^{-\beta}$  is related to the smallest element of the mesh. For uniform meshes, i.e. for  $\beta = 1$ , it is easy to see that  $\ell_{\max} = \ell_{\min} = \ell/L$ . In Table 1, we report the space-time discretization parameters, associated to the decomposition of the computational domain for  $\beta = 1, 2$ .

$L$	$\Delta_t$	$N_{\Delta_t}$	$\ell_{\max} = \ell_{\min} \ (\beta = 1)$	$\ell_{\max} \ (\beta = 2)$	$\ell_{\min} \ (\beta = 2)$	$M_{\Delta_{\mathbf{x}}}$
2	$2.5000e-01$	4	$2.5000e-01$	$3.7500e-01$	$1.2500e-01$	32
4	$1.2500e-01$	8	$1.2500e-01$	$2.1875e-01$	$3.1250e-02$	128
8	$6.2500e-02$	16	$6.2500e-02$	$1.1719e-01$	$7.8125e-03$	512
16	$3.1250e-02$	32	$3.1250e-02$	$6.0547e-02$	$1.9531e-03$	2048
32	$1.5625e-02$	64	$1.5625e-02$	$3.0762e-02$	$4.8828e-04$	8192

Table 1: Example 1. Discretization parameters of the square screen  $\beta$ -meshes with  $\beta = 1$  and  $\beta = 2$ , for different values of  $L$ .

In Figure 2 the meshes corresponding to the  $L = 16$  are represented for  $\beta = 1$  (left plot) and  $\beta = 2$  (right plot).

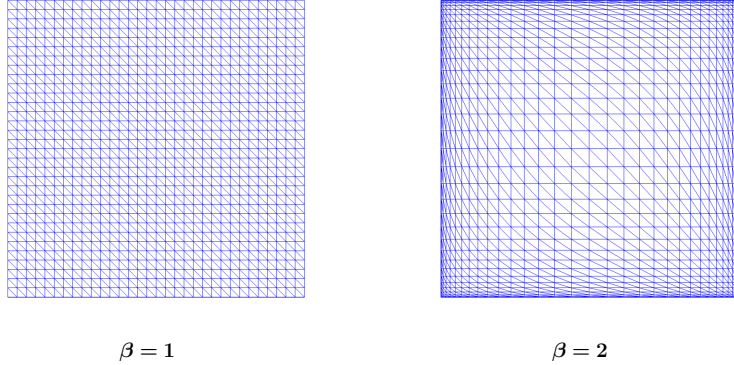


Figure 2: Example 1. Meshes of  $\Gamma$  corresponding to  $L = 16$ , for  $\beta = 1$  (left plot) and  $\beta = 2$  (right plot).

Figure 3 shows the component in the  $x_3$ -direction of the numerical solution  $\mathbf{w}_{\Delta_{\mathbf{x}}, \Delta_t}$  (the only non-trivial one) on  $\Gamma$  in the scaled left plot and along a cross-section in the right plot at the final time. Here, a 2-graded mesh with  $L = 32$  was used.

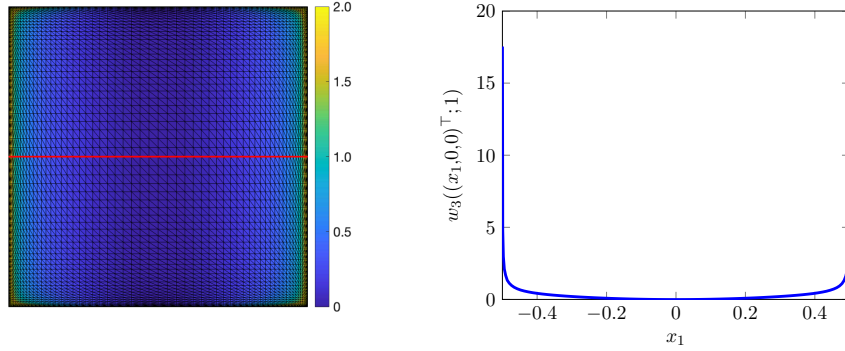


Figure 3: Example 1. For the  $\beta$ -graded mesh with  $\beta = 2$  and  $L = 32$ , component in  $x_3$ -direction of the numerical solution  $\mathbf{w}_{\Delta_x, \Delta_t}$  at the final time  $T = 1$  on  $\Gamma$  (scaled left plot) and along  $x_2 = 0$  (right plot).

Moreover, the asymptotic behavior of the numerical solutions for  $\beta = 1, 2$ ,  $L = 32$ , at  $T = 1$ , is shown in Figure 4, along the  $x_1$ -axis, for  $x_2 = x_3 = 0$ . Here, the horizontal axis uses the distance  $r$  from the left side of the screen. The singular behavior of the numerical solution on the 2-graded mesh (green line), respectively, on the uniform mesh (blue line), agrees with the theoretically predicted behavior from Section 3.4, i.e.  $\mathcal{O}(r^{-1/2})$  (dashed red line).

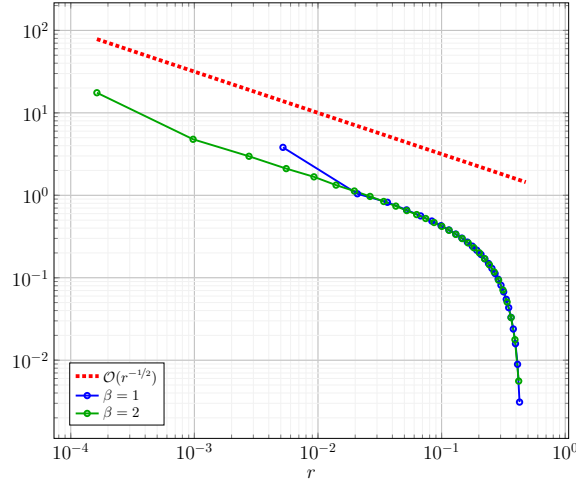


Figure 4: Example 1. Asymptotic behavior of the numerical solution ( $L = 32$ ) along the  $x_1$ -axis, at  $T = 1$ , for  $\beta = 1, 2$ . The plot is with respect to the distance  $r$  from the left side of the screen.

In Figure 5 we depict the asymptotic behavior of the numerical solution at  $T = 1$  for different ratios between primary and secondary wave speeds, again for  $\beta = 2$  and  $L = 32$ . The left plot depicts the numerical solution along the  $x_1$ -axis with respect to the distance  $r$  from the left side of the screen. The behavior  $\mathcal{O}(r^{-0.5})$  is independent of the elastodynamic parameters, as theoretically discussed in Section 3.4. Similarly, the right plot depicts the numerical solution along the line  $x_2 = -x_1$  with respect to the distance from the top-left corner. The singular behavior  $\mathcal{O}(r^{-0.78})$  is independent of the elastodynamic parameters and in line with the theoretical analysis in Section 3.4. The qualitative behavior agrees with that obtained for the scalar wave equation in [22].

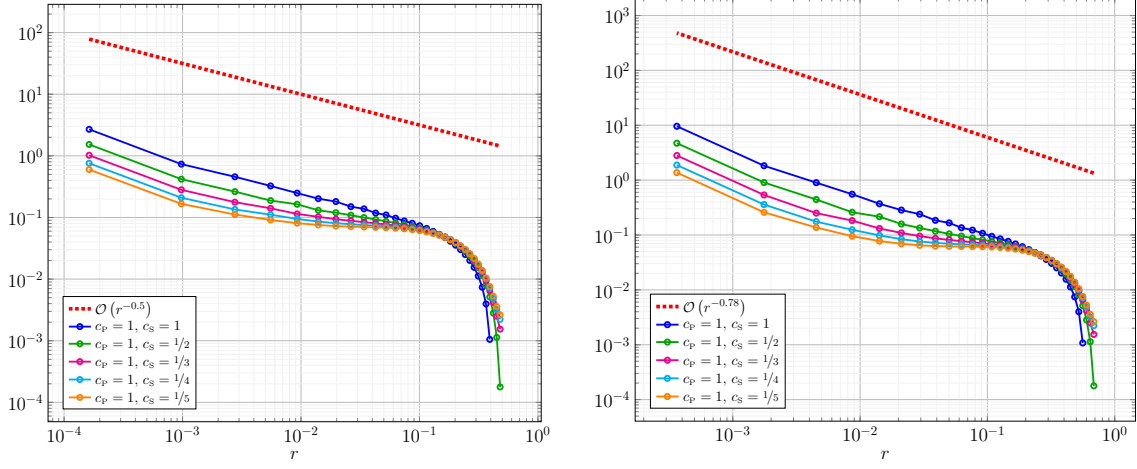


Figure 5: Example 1. Asymptotic behavior of the numerical solution ( $L = 32$ ) along the  $x_1$ -axis (left plot) and along the line  $x_2 = -x_1$  (right plot), at  $T = 1$ , for  $\beta = 2$  and different ratios between primary and secondary wave speeds. The plot is with respect to the distance  $r$  from the screen boundary.

In Table 2 we report the values of the squared energy  $\mathcal{E}_L := \mathcal{E}(\mathbf{w}_L)$  of the numerical solution. Figure 6 presents the squared energy errors with respect to the common benchmark  $\mathcal{E}_\infty = 0.0145377$ , which was obtained by extrapolation from the energy values for  $\beta = 2$ . The convergence rate  $\simeq \beta$  is in very good agreement with the theoretical prediction from Section 5.2.

$L$	$\parallel$	2	4	8	16	32
$\mathcal{E}_L (\beta = 1)$	$\parallel$	$1.1518e - 02$	$1.3088e - 02$	$1.3804e - 02$	$1.4162e - 02$	$1.4345e - 02$
$\mathcal{E}_L (\beta = 2)$	$\parallel$	$1.2867e - 02$	$1.4197e - 02$	$1.4458e - 02$	$1.4519e - 02$	$1.4533e - 02$

Table 2: Example 1. Squared energy values of the numerical solution at  $T = 1$  for  $\beta = 1, 2$  and different values of  $L$ .

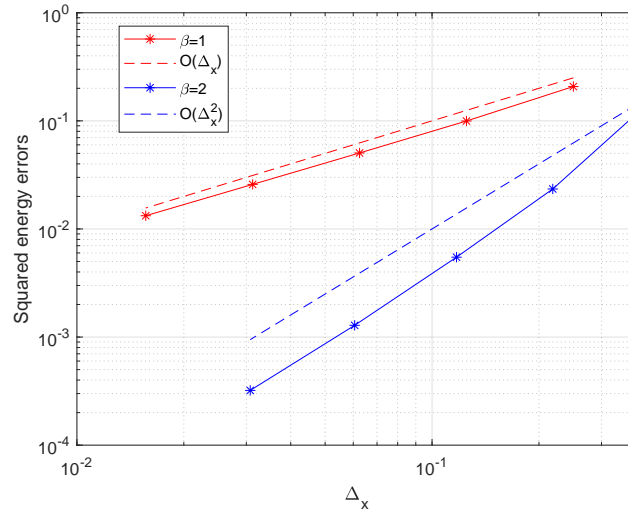


Figure 6: Example 1. Squared errors in energy norm for  $\beta = 1$  and  $\beta = 2$ .



**Example 2. Circular screen.** We consider  $\Gamma := \{x_1^2 + x_2^2 \leq R^2\} \times \{x_3 = 0\}$ , with  $R = 0.5$ . Here the radial nodes in the  $\beta$ -graded mesh are given by  $r_k = R(1 - (\frac{k}{L})^\beta)$ ,  $k = 0, \dots, L$  and the number of angular elements is increased towards the boundary as shown in Figure 7, where the meshes corresponding to  $L = 8$  are represented for  $\beta = 1$  (left plot),  $\beta = 2$  (center plot) and  $\beta = 3$  (right plot).

The parameters  $\ell_{\max}$  and  $\ell_{\min}$  for  $\beta = 1, 2$  are the same as in Table 1, while for  $\beta = 3$  they are shown in Table 3, together with the remaining discretization parameters.

$L$	$\Delta_t$	$N_{\Delta_t}$	$\ell_{\max} (\beta = 3)$	$\ell_{\min} (\beta = 3)$	$M_{\Delta_{\mathbf{x}}}$
2	$2.5000e - 01$	4	$4.3750e - 01$	$6.2500e - 02$	16
4	$1.2500e - 01$	8	$2.8906e - 01$	$7.8125e - 03$	128
8	$6.2500e - 02$	16	$1.6504e - 01$	$9.7656e - 04$	1024
16	$3.1250e - 02$	32	$8.8013e - 02$	$1.2207e - 04$	8192

Table 3: Example 2. Discretization parameters of the circular screen  $\beta$ -mesh with  $\beta = 3$ . for different values of  $L$ .

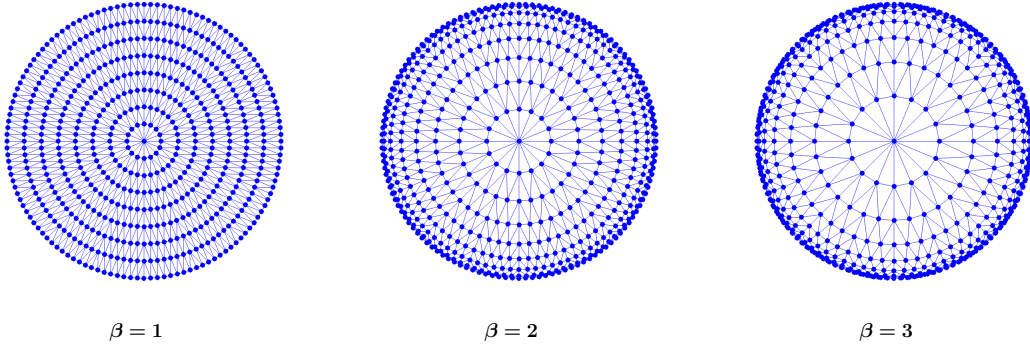


Figure 7: Example 2. Meshes of  $\Gamma$  corresponding to  $L = 8$ , for  $\beta = 1$  (left plot),  $\beta = 2$  (center plot) and  $\beta = 3$  (right plot).

Figure 8 shows the component in  $x_3$ -direction of the numerical solution  $\mathbf{w}_{\Delta_{\mathbf{x}}, \Delta_t}$  (the only one not trivial) on  $\Gamma$  (scaled left plot) and along a cross-section (right plot) at the final time. These results are obtained by considering a  $\beta$ -graded mesh with  $\beta = 3$  for  $L = 16$ .

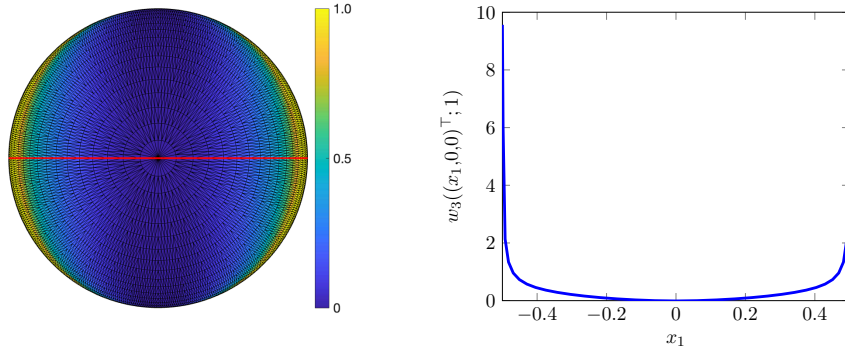


Figure 8: Example 2. For the  $\beta$ -graded mesh with  $\beta = 3$  and  $L = 16$ , component in  $x_3$ -direction of the numerical solution  $\mathbf{w}_{\Delta_{\mathbf{x}}, \Delta_t}$  at the final time  $T = 1$  on  $\Gamma$  (scaled left plot) and along  $x_2 = 0$  (right plot).

Figure 9 shows the asymptotic behavior of the numerical solutions at  $T = 1$  along the  $x_1$ -axis, for  $x_2 = x_3 = 0$ , with respect to the distance  $r$  from the boundary of the circular screen. Here,  $\beta = 1, 2, 3$ ,  $L = 16$ , have been used. The singular behavior of the numerical solutions agrees with the theoretically predicted behavior from Section 3.4, i.e.  $\mathcal{O}(r^{-1/2})$  (dashed red line), particularly for  $\beta = 3$ .

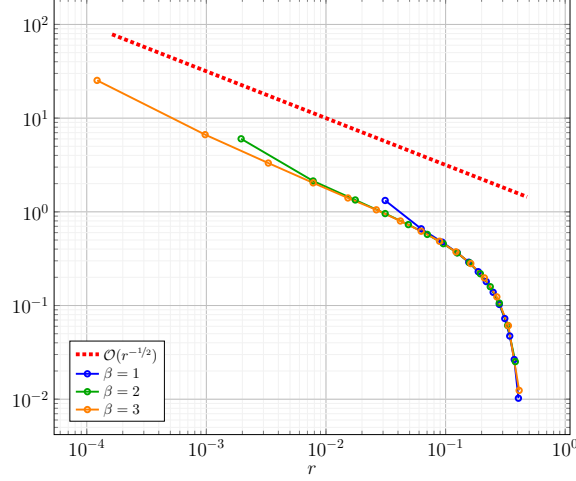


Figure 9: Example 2. Asymptotic behavior of the numerical solution ( $L = 16$ ) along the  $x_1$ -axis, at  $T = 1$ , for  $\beta = 1, 2, 3$ . The plot is with respect to the distance  $r$  from the circular screen boundary.

In Table 4 we report the values of the squared energy  $\mathcal{E}_L$  of the numerical solution. Figure 10 presents the squared energy errors with respect to the common benchmark  $\mathcal{E}_\infty = 0.0071888$ , which was obtained by extrapolation from the energy values for  $\beta = 3$ . Again, the convergence rate  $\simeq \beta$  is in very good agreement with the theoretical prediction from Section 5.2.

$L$	$\parallel$	2	4	6	8	12	16
$\mathcal{E}_L(\beta = 1)$	$\parallel$	$4.0000e - 03$	$6.3122e - 03$	$6.7169e - 03$	$6.8562e - 03$	$6.9901e - 03$	$7.0454e - 03$
$\mathcal{E}_L(\beta = 2)$	$\parallel$	$4.6143e - 03$	$6.8793e - 03$	$7.0906e - 03$	$7.1386e - 03$	$7.1679e - 03$	$7.1751e - 03$
$\mathcal{E}_L(\beta = 3)$	$\parallel$	$4.8380e - 03$	$7.0302e - 03$	$7.1698e - 03$	$7.1860e - 03$	$7.1880e - 03$	$7.1885e - 03$

Table 4: Example 2. Squared energy values of the numerical solution at  $T = 1$  for  $\beta = 1, 2, 3$  and different values of  $L$ .

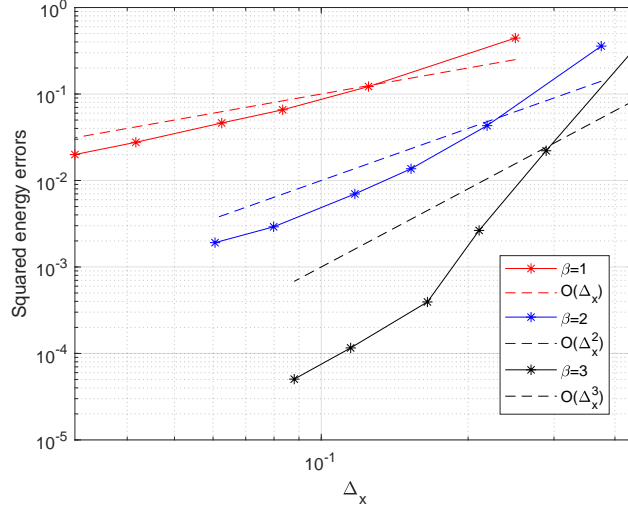


Figure 10: Example 2. Squared errors in energy norm for  $\beta = 1, 2, 3$ .

**Example 3. L-shaped screen.** In this example, we consider  $\Gamma := ([-\ell, \ell]^2 \setminus [0, \ell]^2) \times \{x_3 = 0\}$ , with  $\ell = 0.5$ , and the Dirichlet datum  $\mathbf{g}(\mathbf{x}; t) = (0, 0, [(x_1 + \ell)^2 + (x_2 + \ell)^2] \sin^5 t)^\top$ . The final time is set  $T = 1$ , while the material parameters  $\varrho = 1$ ,  $\mu = 0.25$  and  $\lambda = 0.5$  are taken, in such a way that  $c_p = 1$ ,  $c_s = 0.5$ .

The graded mesh on the L-shape is obtained from three copies of the graded mesh used in Example 1, see Figure 11 for the meshes corresponding to  $L = 16$  with  $\beta = 1$  (left plot),  $\beta = 2$  (center plot) and  $\beta = 3$  (right plot). The discretization parameters for  $\beta = 1, 2$  are shown in Table 5.

$L$	$\Delta_t$	$N_{\Delta_t}$	$\ell_{\max} = \ell_{\min} (\beta = 1)$	$\ell_{\max} (\beta = 2)$	$\ell_{\min} (\beta = 2)$	$M_{\Delta_{\mathbf{x}}}$
2	$1.2500e-01$	8	$1.2500e-01$	$1.8750e-01$	$6.2500e-02$	96
4	$6.2500e-02$	16	$6.2500e-02$	$1.0938e-01$	$1.5625e-02$	384
8	$3.1250e-02$	32	$3.1250e-02$	$5.8594e-02$	$3.9062e-03$	1536
16	$1.5625e-02$	64	$1.5625e-02$	$3.0273e-02$	$9.7656e-04$	6144

Table 5: Example 3. Discretization parameters of the L-shaped screen  $\beta$ -meshes with  $\beta = 1$  and  $\beta = 2$ , for different values of  $L$ .

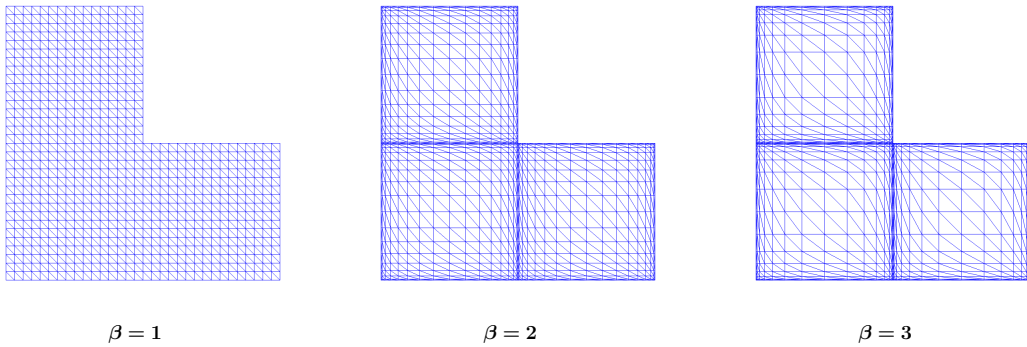


Figure 11: Example 3. Meshes of  $\Gamma$  corresponding to  $L = 16$ , for  $\beta = 1$  (left plot),  $\beta = 2$  (center plot) and  $\beta = 3$  (right plot).

Figure 12 shows the component in  $x_3$ -direction of the numerical solution  $\mathbf{w}_{\Delta_{\mathbf{x}}, \Delta_t}$  (the only one not trivial) on  $\Gamma$  (scaled left-top plot) and along three cross-sections (right-top plot along the red diagonal, left-bottom plot along the green segment on the  $x_1$  axis, right-bottom plot along the magenta diagonal) at the final time. These results are obtained on a  $\beta$ -graded mesh with  $\beta = 3$  for  $L = 16$ . We observe the singular behavior of the numerical solution towards the screen boundary, with different orders of magnitude, except towards the left-bottom corner, where the solution is trivial.

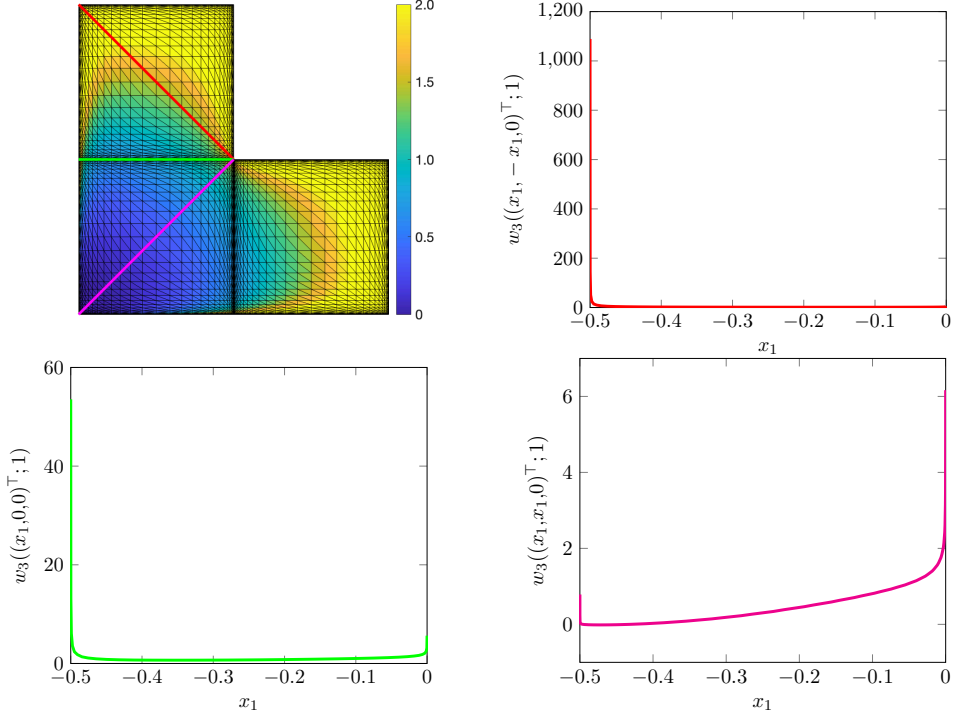


Figure 12: Example 3. For the  $\beta$ -graded mesh with  $\beta = 3$  and  $L = 16$ , component in  $x_3$ -direction of the numerical solution  $\mathbf{w}_{\Delta_{\mathbf{x}}, \Delta_t}$  at the final time  $T = 1$  on  $\Gamma$  (scaled left-top plot) and along three cross-sections (right-top plot along the red diagonal, left-bottom plot along the green segment on the  $x_1$  axis, right-bottom plot along the magenta diagonal).

Figure 13 shows the asymptotic behavior of the numerical solutions at  $T = 1$  with respect to the distance  $r$  from the left side of the screen, along the green line (on the left) and along the red line (in the center) highlighted on the L-shaped screen and from the re-entrant corner along the red, green and magenta lines (on the right). Here,  $\beta = 3$ ,  $L = 16$ , have been used. The behavior of the green curve on the left plot is  $O(r^{-1/2})$ . The red curve in the central plot has a steeper slope  $O(r^{-3/4})$ , while the three curves on the right plot behave approximately as  $O(r^{-1/4})$ .

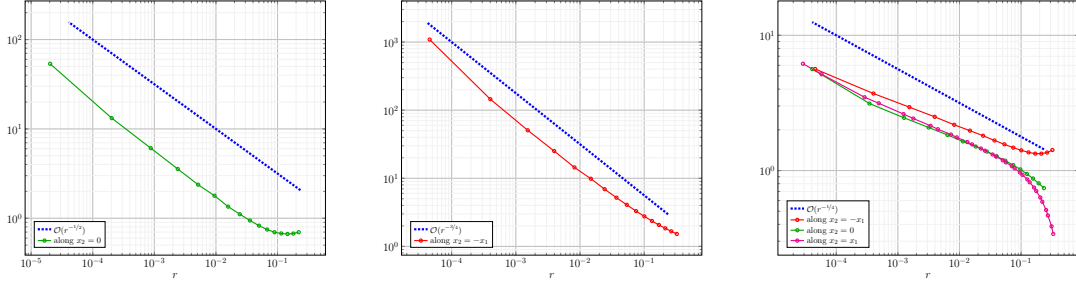


Figure 13: Example 3. Asymptotic behavior of the numerical solution ( $L = 16$ ) for  $\beta = 3$ , along the red, green and magenta lines highlighted in the L-shaped screen. The plot on the right is with respect to the distance  $r$  from the left side of the screen, the plot in the center is with respect to the distance  $r$  from the top-left corner, while the plot on the right is with respect to the distance  $r$  from the re-entrant corner.

In Table 6 we report the values of the squared energy  $\mathcal{E}_L$  of the numerical solution. Figure 14 presents the squared energy errors with respect to the common benchmark  $\mathcal{E}_\infty = 0.27029$ , which was obtained by extrapolation from the energy values for  $\beta = 3$ . Again, the convergence rate  $\simeq \beta$  is in very good agreement with the theoretical prediction from Section 5.2. Note that the optimal convergence rate is obtained for  $\beta = 3$ .

$L$	$\parallel$	2	4	6	8	12	16
$\mathcal{E}_L(\beta = 1)$	$\parallel$	$2.5292e - 01$	$2.6092e - 01$	$2.6380e - 01$	$2.6531e - 01$	$2.6688e - 01$	$2.6768e - 01$
$\mathcal{E}_L(\beta = 2)$	$\parallel$	$2.6034e - 01$	$2.6767e - 01$	$2.6907e - 01$	$2.6957e - 01$	$2.6995e - 01$	$2.7008e - 01$
$\mathcal{E}_L(\beta = 3)$	$\parallel$	$2.6504e - 01$	$2.6961e - 01$	$2.7015e - 01$	$2.7024e - 01$	$2.7027e - 01$	$2.7028e - 01$

Table 6: Example 3. Squared energy values of the numerical solution at  $T = 1$  for  $\beta = 1, 2, 3$  and different values of  $L$ .

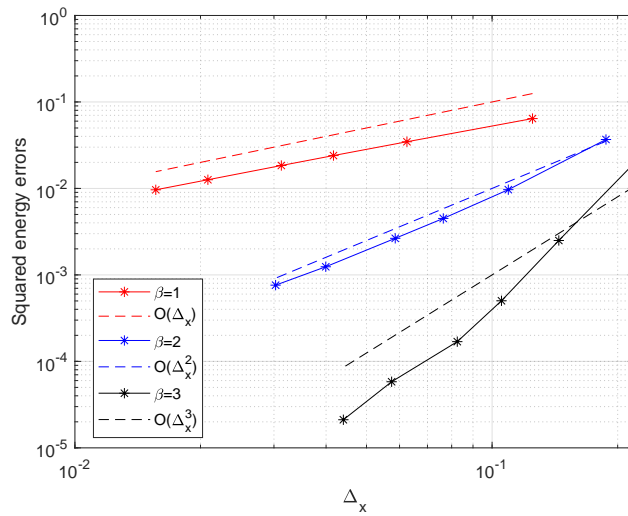


Figure 14: Example 3. Squared errors in energy norm for  $\beta = 1, 2, 3$ .

**Example 4. Cone.** In this example, we consider the cone  $\Gamma := \{(x_1, x_2, x_3) : \sqrt{x_1^2 + x_2^2} \leq$

$R \wedge x_3 = (R - \sqrt{x_1^2 + x_2^2}) \tan(\omega) \cup \{(x_1, x_2, 0) : \sqrt{x_1^2 + x_2^2} \leq R\}$ , where  $\omega = \pi/9$  is the angle between the lateral surface and the disk of radius  $R = 0.5$  centered in the origin of the  $x_1x_2$ -plane, which represents the cone base. The Dirichlet datum is  $\mathbf{g}(\mathbf{x}; t) = (0, 0, \sin^5 t(x_1^2 + x_2^2)/R)^\top$ . The final time is set  $T = 1$ , while the material parameters  $\varrho = 1$ ,  $\mu = 0.25$  and  $\lambda = 0.5$  are taken, in such a way that  $c_P = 1$ ,  $c_S = 0.5$ , as before.

We introduce on the base of the cone a graded mesh as discussed in Example 2, suitably connected to the mesh constructed on the lateral surface of the 3D domain taken into account, graded towards both the apex and the base of the cone. Along the red line on the lateral surface in Figure 15 on the right, the nodes of the mesh have the following coordinates:

$$\begin{aligned} \mathbf{x}_1 &= \mathbf{0} \\ \mathbf{x}_2 &= \left[ R - \frac{R}{2} \left( \frac{[0:1:(L/2-1)]}{L/2} \right)^\beta, \frac{R}{2}, \frac{R}{2} \left( \frac{[(L/2-1):-1:1]}{L/2} \right)^\beta, 0 \right] \\ \mathbf{x}_3 &= \mathbf{x}_2 \tan(\omega) \end{aligned}$$

Some of the employed discretization parameters for  $\beta = 1, 2, 3$  are shown in Table 7.

$L$	$\Delta_t$	$N_{\Delta_t}$	$\ell_{\max}(\beta = 1)$	$\ell_{\max}(\beta = 2)$	$\ell_{\max}(\beta = 3)$	$M_{\Delta_{\mathbf{x}}}$
4	$1.2500e-01$	8	$1.3302e-01$	$2.1875e-01$	$2.8906e-01$	256
6	$8.3333e-02$	12	$8.8681e-02$	$1.5278e-01$	$2.1065e-01$	864
8	$6.2500e-02$	16	$6.6511e-02$	$1.1719e-01$	$1.6504e-01$	2048
12	$4.1667e-02$	24	$4.4341e-02$	$8.1291e-02$	$1.1487e-01$	6912

Table 7: Example 4. Discretization parameters of the cone surface  $\beta$ -meshes with  $\beta = 1, 2, 3$ , for different values of  $L$ .

In Figure 15 the meshes corresponding to  $L = 8$  are represented for  $\beta = 1$  (left plot),  $\beta = 2$  (center plot) and  $\beta = 3$  (right plot).

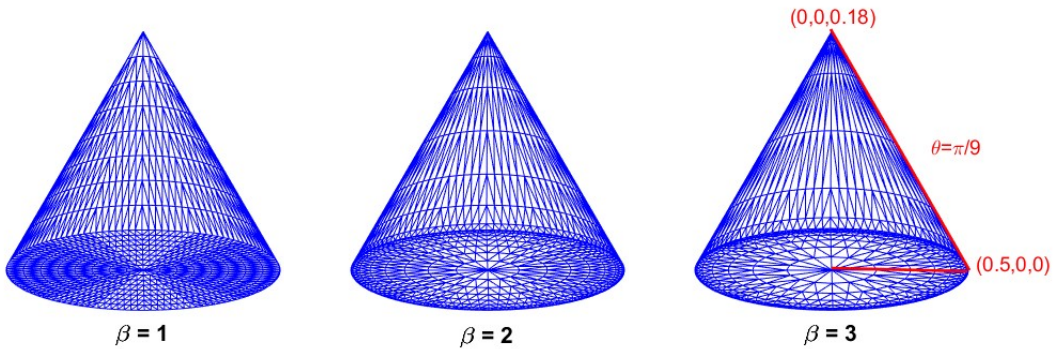


Figure 15: Example 4. Meshes of  $\Gamma$  corresponding to  $L = 8$ , for  $\beta = 1$  (left plot),  $\beta = 2$  (center plot) and  $\beta = 3$  (right plot).

Figure 16 shows the three components of the numerical solution  $\mathbf{w}_{\Delta_{\mathbf{x}}, \Delta_t}$  on  $\Gamma$ , at the final time, using  $\beta = 1$  and  $L = 4$ . We observe the singular behavior of the numerical solution towards the circular boundary of the cone base.

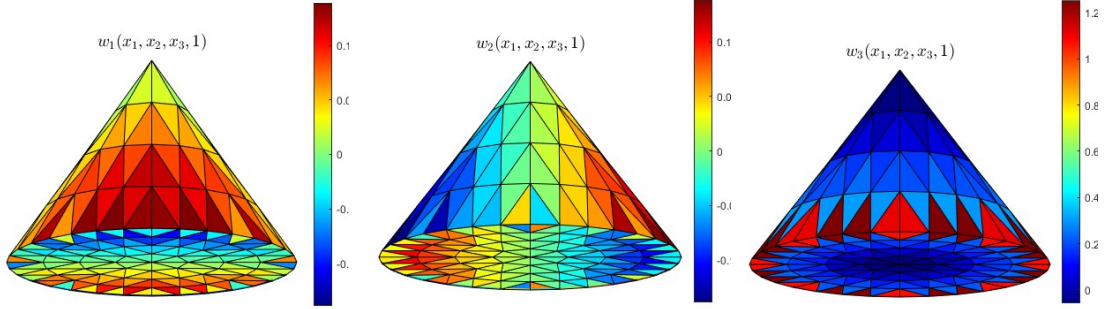


Figure 16: Example 4. For the  $\beta$ -graded mesh with  $\beta = 1$  and  $L = 4$ , from left to right, the components in  $x_1, x_2, x_3$  directions of the numerical solution  $\mathbf{w}_{\Delta_{\mathbf{x}}, \Delta_t}$  at the final time  $T = 1$  on  $\Gamma$ .

Figure 17 shows the numerical solutions at  $T = 1$  with respect to the distance  $r$  from the circular boundary of the cone base, using  $\beta = 1, 2, 3$ ,  $L = 12$ . The singular behavior of the solution is of the form  $O(r^{\alpha-1})$  with  $\alpha = 0.5117$ , due to the wedge type singularity at the base of the cone. The singularity at the cone tip is milder, in agreement with the theoretical analysis from Section 3.

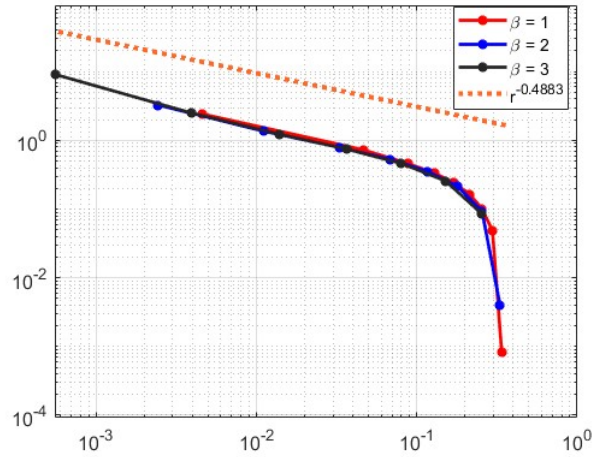


Figure 17: Example 4. Asymptotic behavior of the numerical solution ( $L = 12$ ) for  $\beta = 1, 2, 3$ . The plot is with respect to the distance  $r$  from the circular boundary of the cone base.

In Table 8 we report the values of the squared energy  $\mathcal{E}_L$  of the numerical solution. Figure 18 presents the squared energy errors with respect to the common benchmark  $\mathcal{E}_\infty = 0.078431$ , which was obtained by extrapolation from the energy values for  $\beta = 3$ . Again, the convergence rate  $\simeq \beta$  is in very good agreement with the theoretical prediction from Section 5.2. Note that the optimal convergence rate is obtained for  $\beta = 3$ , in agreement with (5.4).



$L$	$\parallel$	4	6	8	12
$\mathcal{E}_L (\beta = 1)$	$\parallel$	$7.0039e - 02$	$7.4195e - 02$	$7.5435e - 02$	$7.6664e - 02$
$\mathcal{E}_L (\beta = 2)$	$\parallel$	$7.5018e - 02$	$7.7361e - 02$	$7.7864e - 02$	$7.8177e - 02$
$\mathcal{E}_L (\beta = 3)$	$\parallel$	$7.6682e - 02$	$7.8143e - 02$	$7.8332e - 02$	$7.8395e - 02$

Table 8: Example 4. Squared energy values of the numerical solution at  $T = 1$  for  $\beta = 1, 2, 3$  and different values of  $L$ .

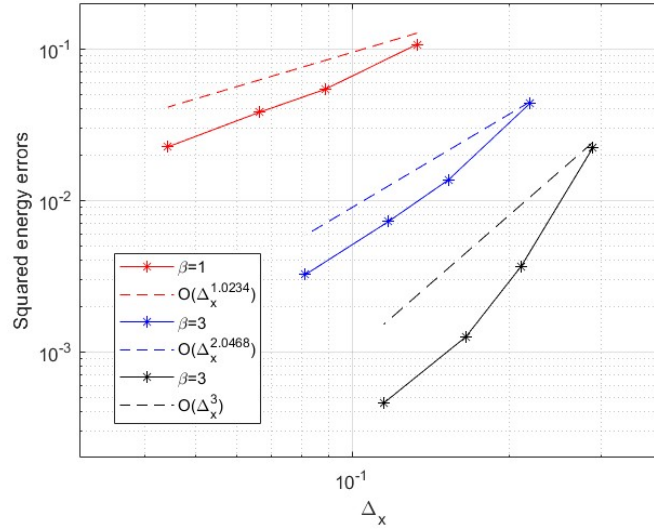


Figure 18: Example 4. Squared errors in energy norm for  $\beta = 1, 2, 3$ .

**Example 5. Top-down ice-cream geometry.** In this example, we consider  $\Gamma := \{(x_1, x_2, x_3) : \sqrt{x_1^2 + x_2^2} \leq R \wedge x_3 = (R - \sqrt{x_1^2 + x_2^2}) \tan(\omega)\} \cup \{(x_1, x_2, x_3) : \sqrt{x_1^2 + x_2^2} \leq R \wedge x_3 = -\sqrt{R^2 - x_1^2 - x_2^2}\}$ , constituted by a cone whose angle with  $x_1x_2$ -plane is  $\omega = 9\pi/20$  with a hemispherical base of radius  $R = 0.5$ . The Dirichlet datum is  $\mathbf{g}(\mathbf{x}; t) = (0, 0, \sin^5 t(1 - (x_1^2 + x_2^2)/R))^T$ . The final time is set  $T = 1$ , while the material parameters  $\varrho = 1$ ,  $\mu = 0.25$  and  $\lambda = 0.5$  are taken, in such a way that  $c_P = 1$ ,  $c_S = 0.5$ , as before.

We introduce on the hemispherical surface graded meshes inherited by the graded meshes on the disk as considered in Example 2, suitably connected to the mesh constructed on the lateral surface of the cone part taken into account, graded, similarly to what happens in Example 4, towards both the apex and the hemisphere. Some of the employed discretization parameters for  $\beta = 1, 2, 3$  are shown in Table 9:

$L$	$\Delta_t$	$N_{\Delta_t}$	$\ell_{\max} (\beta = 1)$	$\ell_{\max} (\beta = 2)$	$\ell_{\max} (\beta = 3)$	$M_{\Delta_x}$
4	$1.2500e - 01$	8	$7.9906e - 01$	$1.1986e + 00$	$1.3983e + 00$	256
6	$8.3333e - 02$	12	$5.3270e - 01$	$8.8784e - 01$	$1.1246e + 00$	864
8	$6.2500e - 02$	16	$3.9953e - 01$	$6.9917e - 01$	$9.2391e - 01$	2048
12	$4.1667e - 02$	24	$2.6635e - 01$	$4.8831e - 01$	$6.7328e - 01$	6912

Table 9: Example 5. Discretization parameters of the domain surface  $\beta$ -meshes with  $\beta = 1, 2, 3$ , for different values of  $L$ .



In Figure 19 the meshes corresponding to  $L = 6$  are represented for  $\beta = 1$  (left plot),  $\beta = 2$  (center plot) and  $\beta = 3$  (right plot).

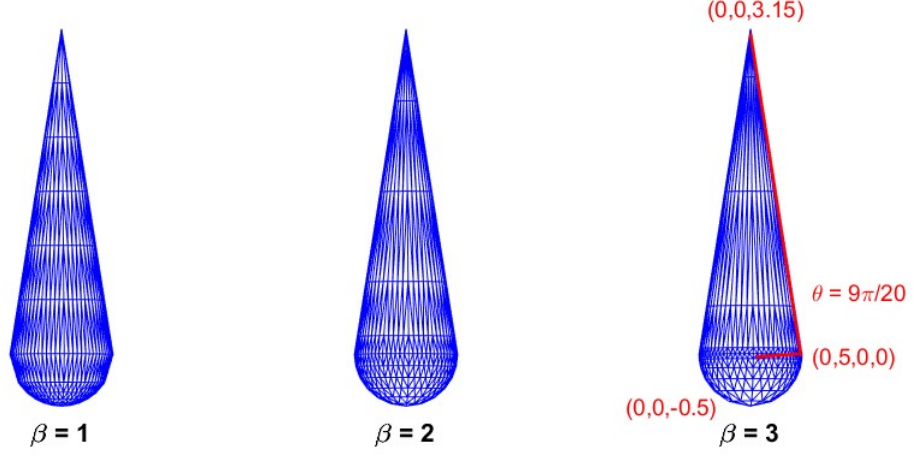


Figure 19: Example 5. Meshes of  $\Gamma$  corresponding to  $L = 6$ , for  $\beta = 1$  (left plot),  $\beta = 2$  (center plot) and  $\beta = 3$  (right plot).

Figure 20 shows the three components of the numerical solution  $\mathbf{w}_{\Delta_{\mathbf{x}}, \Delta_t}$  on  $\Gamma$ , at the final time. These results are obtained by considering a  $\beta$ -graded mesh with  $\beta = 3$  for  $L = 6$ . We observe the singular behavior of the numerical solution towards the apex of the top-down ice-cream geometry.

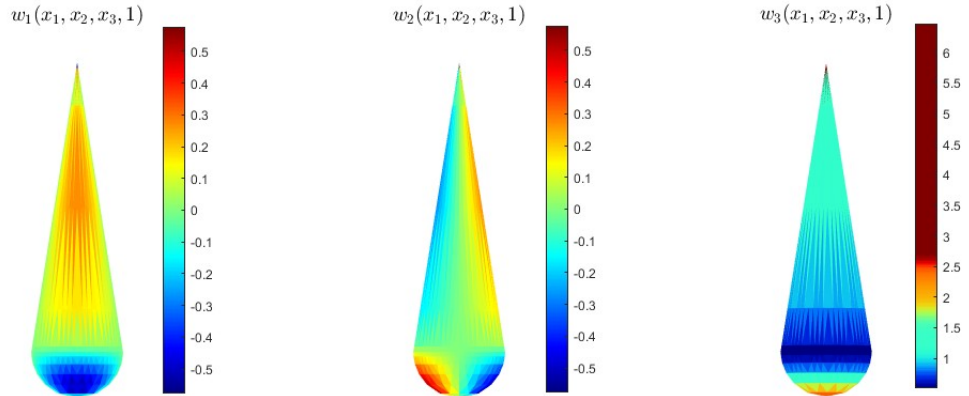


Figure 20: Example 5. For the  $\beta$ -graded mesh with  $\beta = 3$  and  $L = 6$ , from left to right, the components in  $x_1, x_2, x_3$  directions of the numerical solution  $\mathbf{w}_{\Delta_{\mathbf{x}}, \Delta_t}$  at the final time  $T = 1$  on  $\Gamma$ .

Moreover, the singular behavior of the numerical solutions for  $\beta = 1, 2, 3$ ,  $L = 12$ , at  $T = 1$ , is shown in Figure 21. The plot is with respect to the distance  $r$  from the apex of the domain. This behavior turns out to be  $O(r^{\tilde{\alpha}-1})$  with  $\tilde{\alpha} = 0.23189$  due to the prevailing cone (apex) singularity, and follows the theoretical prediction from Section 3.

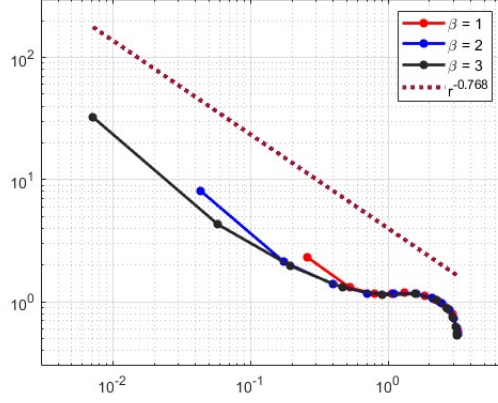


Figure 21: Example 5. Asymptotic behavior of the numerical solution ( $L = 12$ ) for  $\beta = 1, 2, 3$ . The plot is with respect to the distance  $r$  from the apex of the domain.

In Table 10 we report the values of the squared energy  $\mathcal{E}_L$  of the numerical solution. Figure 22 presents the squared energy errors with respect to the common benchmark  $\mathcal{E}_\infty = 1.5153$ , which was obtained by extrapolation from the energy values for  $\beta = 3$ . Again, the convergence rate  $\simeq \beta$  is in very good agreement with the theoretical prediction from Section 5.2. Note that the optimal convergence rate is obtained for  $\beta = 3$ , as can be deduced from (5.4) with  $\alpha = \tilde{\alpha} + 1/2 = 0.73189$ .

$L$	$\parallel$	4	6	8	12
$\mathcal{E}_L$ ( $\beta = 1$ )	$\parallel$	$1.4847e + 00$	$1.5023e + 00$	$1.5079e + 00$	$1.5117e + 00$
$\mathcal{E}_L$ ( $\beta = 2$ )	$\parallel$	$1.4908e + 00$	$1.5060e + 00$	$1.5106e + 00$	$1.5135e + 00$
$\mathcal{E}_L$ ( $\beta = 3$ )	$\parallel$	$1.4901e + 00$	$1.5067e + 00$	$1.5115e + 00$	$1.5142e + 00$

Table 10: Example 5. Squared energy values of the numerical solution at  $T = 1$  for  $\beta = 1, 2, 3$  and different values of  $L$ .

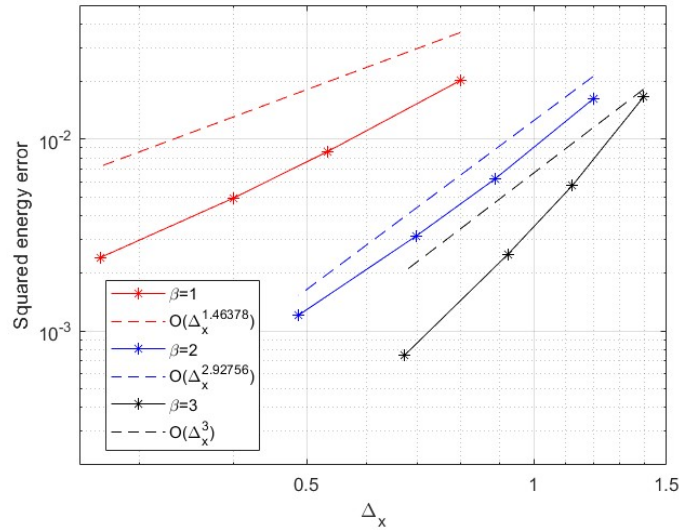


Figure 22: Example 5. Squared errors in energy norm for  $\beta = 1, 2, 3$ .

## 7 Conclusions

This article reduced boundary value problems for 3D time-domain elastodynamics, endowed with a Dirichlet type boundary and null initial conditions, to time dependent weakly singular boundary integral equations. Guided by the singular behavior of the solution near cone points, corners and edges proposed in [4], we have numerically studied a space-time energetic boundary element method on graded meshes. Extensive numerical results confirmed the performance of the approach and the theoretically predicted, quasi-optimal convergence rates. The singular behavior of the solutions is reliably computed, allowing a study of the singular exponents for the time dependent elastic problem.

## Acknowledgments

Parts of this research were supported by the Research in Residence program of the Centre International de Rencontres Mathématiques, Luminy, in 2023. This work was performed as part of the GNCS-INdAM 2025 research program *High-order BEM based numerical techniques for wave propagation problems* (CUP E53C24001950001). Luca Desiderio acknowledges the financial support provided by the European Union *Next GenerationEU*, in the framework of the project *Strategie HPC e modelli fisico-numerici per la previsione di eventi meteorologici estremi* (HPC-XTREME) from the National Recovery and Resilience Plan, Mission 4 'Istruzione e ricerca' Component 2 'Dalla ricerca alla impresa'- Investment 1.4 - NATIONAL CENTER FOR HPC, BIG DATA AND QUANTUM COMPUTING (Project Code CN00000013 - CUP B83C22002830001). The views and opinions expressed are solely those of the authors and do not necessarily reflect those of the European Union, nor can the European Union be held responsible for them.

## Appendix

Let  $L^2(\tilde{\Gamma})$  be the space of measurable functions whose square is Lebesgue integrable on  $\tilde{\Gamma}$ . The inner product and the norm of this space are defined respectively by:

$$\langle u, v \rangle_{L^2(\tilde{\Gamma})} := \int_{\tilde{\Gamma}} u(\mathbf{x})v(\mathbf{x})d\Gamma_{\mathbf{x}} \quad \text{and} \quad \|u\|_{L^2(\tilde{\Gamma})} := \sqrt{\langle u, u \rangle_{L^2(\tilde{\Gamma})}} \quad \forall u, v \in L^2(\tilde{\Gamma}).$$

Now, we recall that at each point  $\mathbf{x} \in \tilde{\Gamma}$  there is an open neighbourhood  $U$  and a bijective mapping  $\phi : U \rightarrow \mathcal{Q}$ , where  $\mathcal{Q} \subset \mathbb{R}^3$  is the unit cube centered at the origin. Consequently,  $\tilde{\Gamma}$  can be covered by a finite set  $\{U_i\}_{i=1}^k$  of such neighbourhoods, whose corresponding maps form a finite family of diffeomorphisms  $\{\phi_i\}_{i=1}^k$ . If we denote by  $\{\alpha_i\}_{i=1}^k$  a partition of unity subordinate to the covering  $\{U_i\}_{i=1}^k$ , any function  $u : \tilde{\Gamma} \rightarrow \mathbb{R}$  can be written in the form

$$u(\mathbf{x}) = \sum_{i=1}^k \alpha_i(\mathbf{x})u(\mathbf{x}) \quad \forall \mathbf{x} \in \tilde{\Gamma}$$

and each summand can be parametrized over  $\phi_i(U_i \cap \tilde{\Gamma}) \subset \mathbb{R}^2$  as  $(\alpha_i u) \circ \phi_i^{-1}$ . After these preparatory remarks, for each  $s \in \mathbb{R}$  we introduce the Sobolev space

$$H^s(\tilde{\Gamma}) := \left\{ u : \tilde{\Gamma} \rightarrow \mathbb{R} \mid (\alpha_i u) \circ \phi_i^{-1} \in H^s(\phi_i(U_i \cap \tilde{\Gamma})), \forall i = 1, \dots, k \right\}$$

that becomes a Hilbert space once it is equipped with the norm

$$\|u\|_{s, \tilde{\Gamma}} := \sqrt{\sum_{i=1}^k \|(\alpha_i u) \circ \phi_i^{-1}\|_{H^s(\phi_i(U_i \cap \tilde{\Gamma}))}^2}.$$

The value of the above norm clearly depends on the choice of  $U_{i_2} \alpha_i$  and  $\phi_i$ , but one can show that the resulting norms will be equivalent and that the space  $H^s(\tilde{\Gamma})$  is independent of this choice. Furthermore, for every parameter  $\omega = \rho + i\sigma \in \mathbb{C} \setminus \{0\}$ , we introduce  $\omega$ -dependent norms for  $H^s(\tilde{\Gamma})$ , i.e.

$$\|u\|_{s,\omega,\tilde{\Gamma}} := \sqrt{\sum_{i=1}^k \int_{\mathbb{R}^2} (|\omega|^2 + |\xi|^2)^s |\mathcal{F}\{(\alpha_i u) \circ \phi_i^{-1}\}(\xi)|^2 d\xi}$$

where  $\mathcal{F}$  stands for the Fourier transform. Note that, by varying  $\omega$ , each  $\|\cdot\|_{s,\omega,\tilde{\Gamma}}$  is equivalent to  $\|\cdot\|_{s,\tilde{\Gamma}}$ .

At this stage, we call  $\tilde{H}^s(\Gamma)$  the closed subspace of  $H^s(\tilde{\Gamma})$  collecting all the distributions with support in  $\bar{\Gamma}$ , and we denote by  $H^s(\Gamma)$  the quotient space  $H^s(\tilde{\Gamma})/\tilde{H}^s(\tilde{\Gamma} \setminus \bar{\Gamma})$ . We use the norm  $\|\cdot\|_{s,\omega,\tilde{\Gamma}}$  in order to define a norm on  $H^s(\tilde{\Gamma})$ , i.e.

$$\|u\|_{s,\omega,\Gamma} := \inf_{h \in \tilde{H}^s(\tilde{\Gamma} \setminus \bar{\Gamma})} \|u + h\|_{s,\omega,\tilde{\Gamma}} \quad \forall u \in H^s(\tilde{\Gamma}).$$

and a norm on  $H^s(\Gamma)$ , i.e.

$$\|u\|_{s,\omega,\Gamma,*} := \|e^+(u)\|_{s,\omega,\tilde{\Gamma}} \quad \forall u \in H^s(\Gamma),$$

$e^+$  being the operator that extends the distribution  $f$  by 0 from  $\Gamma$  to  $\tilde{\Gamma}$ . Note that, for a fixed  $\omega$ , the norm  $\|\cdot\|_{s,\omega,\Gamma,*}$  is stronger than  $\|\cdot\|_{s,\omega,\Gamma}$ , whenever  $s \in \frac{1}{2} + \mathbb{Z}$ .

For a given  $\sigma > 0$  and two parameters  $s, p \in \mathbb{R}$ , we define the space-time anisotropic Sobolev spaces:

$$\begin{aligned} H_\sigma^p(\mathbb{R}^+; H^s(\Gamma)) &:= \left\{ f \in \mathcal{D}'_+(\mathbb{R}^+; H^s(\Gamma)) : e^{-\text{Im}\{\omega\}t} f \in \mathcal{S}'_+(\mathbb{R}^+; H^s(\Gamma)) \text{ and } \|f\|_{s,\omega,\Gamma} < +\infty \right\} \\ H_\sigma^p(\mathbb{R}^+; \tilde{H}^s(\Gamma)) &:= \left\{ f \in \mathcal{D}'_+(\mathbb{R}^+; \tilde{H}^s(\Gamma)) : e^{-\text{Im}\{\omega\}t} f \in \mathcal{S}'_+(\mathbb{R}^+; \tilde{H}^s(\Gamma)) \text{ and } \|f\|_{s,\omega,\Gamma,*} < +\infty \right\} \end{aligned}$$

where  $\mathcal{D}'_+(E)$  denotes the space of all the distributions on  $\mathbb{R}$  with support in  $[0, +\infty)$ , taking values in a Hilbert space  $E$ , while its subspace  $\mathcal{S}'_+(E) \subset \mathcal{D}'_+(E)$  contains all the tempered distributions. In these two spaces the norms are given respectively by:

$$\begin{aligned} \|f\|_{p,s,\Gamma} &:= \sqrt{\int_{-\infty+i\sigma}^{+\infty+i\sigma} |\omega|^{2p} \|\mathcal{F}\{f\}(\omega)\|_{s,\omega,\Gamma}^2 d\omega} \\ \|f\|_{p,s,\Gamma,*} &:= \sqrt{\int_{-\infty+i\sigma}^{+\infty+i\sigma} |\omega|^{2p} \|\mathcal{F}\{f\}(\omega)\|_{s,\omega,\Gamma,*}^2 d\omega}. \end{aligned}$$

We remark that, for  $p = s = 0$ ,  $H_\sigma^p(\mathbb{R}^+; H^s(\Gamma))$  and  $H_\sigma^p(\mathbb{R}^+; \tilde{H}^s(\Gamma))$  correspond to the weighted  $L^2$ -space with standard inner product. For 3D vector-valued functions in space variable, we denote by  $H_\sigma^p(\mathbb{R}^+; H^s(\Gamma))^3$  and  $H_\sigma^p(\mathbb{R}^+; \tilde{H}^s(\Gamma))^3$  the extension of the previously introduced functional spaces.

## References

- [1] A. Aimi, M. Diligenti, C. Guardasoni, I. Mazzieri, S. Panizzi, *An energy approach to space-time Galerkin BEM for wave propagation problems*, International Journal for Numerical Methods in Engineering, **80**(9), (2009), 1196–1240.

- [2] A. Aimi, M. Diligenti, A. Frangi, C. Guardasoni, *Energetic BEM-FEM coupling for wave propagation in 3D multidomains*, International Journal for Numerical Method in Engineering, **97**, (2014), 377–394.
- [3] A. Aimi, S. Dallospedale, L. Desiderio, C. Guardasoni, *A space-time Energetic BIE method for 3D Elastodynamics. The Dirichlet case*, Computational Mechanics, **72**, (2023), 885–905.
- [4] A. Aimi, G. Di Credico, H. Gimperlein, E. P. Stephan, *Higher-order time domain boundary elements for elastodynamics - graded meshes and hp-versions*, Numerische Mathematik, **154**, (2023), 35–101.
- [5] H. Antes, *A boundary element procedure for transient wave propagations in two-dimensional isotropic elastic media*, Finite Elements in Analysis and Design 1 (1985), 313–322.
- [6] T. Apel, V. Mehrmann, D. Watkins, *Structured eigenvalue methods for the computation of corner singularities in 3D anisotropic elastic structures*, Computer Methods in Applied Mechanics and Engineering, **191**, (2002), 4459–4473.
- [7] T. Apel, A.-M. Sändig, S. I. Solov’ev, *Computation of 3D vertex singularities for linear elasticity: Error estimates for a finite element method on graded meshes*, ESAIM: Mathematical Modelling and Numerical Analysis, **36**, (2002), 1043–1070.
- [8] L. Banjai, F.-J. Sayas, *Integral equation methods for evolutionary PDE*, Springer Ser. Comput. Math., Springer, Cham, 2021.
- [9] Z. P. Bazant, L. M. Keer, *Singularities of elastic stresses and of harmonic functions at conical notches or inclusions*, International Journal of Solids and Structures, **10**, (1974), 957–964.
- [10] E. Bécache, *A variational boundary integral equation method for an elastodynamic antiplane crack*, Internat. J. Numer. Methods Engrg. 36 (1993) 969–984.
- [11] E. Bécache, T. Ha Duong, *A space-time variational formulation for the boundary integral equation in a 2d elastic crack problem*, ESAIM Math. Model. Numer. Anal. 28 (1994) 141–176.
- [12] A. E. Beagles, A.-M. Sändig, *Singularities of Rotationally Symmetric Solutions of Boundary Value Problems for the Lamé Equations*, Z. angew. Math. Mech. 71 (1991), 423–431.
- [13] S. Chaillat, M. Bonnet, *Recent advances on the fast multipole accelerated boundary element method for 3D time-harmonic elastodynamics*, Wave Motion 50 (2013) 1090–1104.
- [14] D. Colton. *Partial Differential Equations: An Introduction*. New York: Random House, 1988.
- [15] M. Costabel, M. Dauge, Z. Yosibash, *A quasilocal function method for extracting edge stress intensity functions*, SIAM Journal on Mathematical Analysis 35 (2004), 1177–1202.
- [16] M. Costabel, F.-J. Sayas, *Time-dependent problems with the boundary integral equation method*, Encyclopedia of Computational Mechanics, Second Edition (ed. E. Stein, R. de Borst, T. J. R. Hughes), John Wiley & Sons, Hoboken, NJ, 2017.
- [17] M. Dauge, *Elliptic boundary value problems in corner domains*, Lecture Notes in Mathematics 1341, Springer-Verlag, 1988.
- [18] L. Desiderio, *An  $\mathcal{H}$ -matrix based direct solver for the Boundary Element Method in 3D elastodynamics*, AIP Conference Proceedings, **1978**, (2018), 120005.
- [19] G. Evans. *Partial Differential Equations*. Springer Undergraduate Mathematics Series. Springer, 1998.

- [20] S. Falletta, G. Monegato, L. Scuderi, *Two boundary integral equation methods for linear elastodynamics*, IMA Journal of Numerical Analysis, **34**(1), (2014), 390–434.
- [21] H. Gimperlein, M. Maischak, E. P. Stephan, *Adaptive time domain boundary element methods and engineering applications*, Journal of Integral Equations and Applications 29 (2017), 75–105.
- [22] H. Gimperlein, F. Meyer, C. Özdemir, D. Stark, E.P. Stephan. *Boundary elements with mesh refinements for the wave equation*, Numerische Mathematik, **139** (2018), 867–912.
- [23] H. Gimperlein, C. Özdemir, D. Stark, E.P. Stephan. *hp-version time domain boundary elements for the wave equation on quasi-uniform meshes*, Computer Methods in Applied Mechanics and Engineering, **356** (2019), 145–174.
- [24] P. Grisvard, *Edge behavior of the solution of an elliptic problem*, Math. Nachr. 132 (1987), 281–299.
- [25] P. Grisvard, *Singularités en élasticité*, Arch. Rational Mech. Anal. 107 (1989), 157–180.
- [26] R.B. Guenther, J.W. Lee. *Partial Differential Equations of Mathematical Physics and Integral Equations*. Inglewood Cliffs, NJ: Prentice-Hall, 1988.
- [27] J. Gwinner, E. P. Stephan, *Advanced Boundary Element Methods – Treatment of Boundary Value, Transmission and Contact Problems*, Springer Series in Computational Mathematics, vol. 52, 2018.
- [28] T. Ha Duong, *On retarded potential boundary integral equations and their discretizations*, in: Topics in computational wave propagation, pp. 301–336, Lect. Notes Comput. Sci. Eng., 31, Springer, Berlin, 2003.
- [29] V. A. Kondratiev, *Boundary value problems for elliptic equations in domains with conical or angular points*, Trans. Moscow Math. Soc. 16 (1967), 227–313.
- [30] D. Korikov, B. Plamenevskii, O. Sarafanov, *Asymptotic theory of dynamic boundary value problems in irregular domains*, Operator Theory: Advances and Applications, vol. 284, Springer Nature, 2021.
- [31] S. I. Matyukevich, B. A. Plamenevskii, *Elastodynamics in domains with edges*, St. Petersburg Math. J. 18 (2007), 459–510.
- [32] F. Müller, C. Schwab, *Finite elements with mesh refinement for elastic wave propagation in polygons*, Math. Methods Appl. Sci. 39 (2016), 5027–5042.
- [33] L. Monasse, C. Mariotti, *An energy-preserving discrete element method for elastodynamics*, ESAIM: Mathematical Modelling and Numerical Analysis, **46**, (2012), 1527–1553.
- [34] N. Omer, Z. Yosibash, *Singular asymptotic expansion of the elastic solution along an edge around which material properties depend on the angular coordinate*, Mathematics and Mechanics of Solids 22 (2017), 2288–2308.
- [35] T. von Petersdorff, E.P. Stephan, *Regularity of mixed boundary value problems in  $\mathbb{R}^3$  and boundary element methods on graded meshes*, Mathematical Methods in the Applied Sciences, **12**, (1990), 229–249.
- [36] M. Schanz, W. Ye, J. Xiao, *Comparison of the convolution quadrature method and enhanced inverse FFT with application in elastodynamic boundary element method*, Comput. Mech. 57 (2016) 523–536.
- [37] C. Schwab, *p- and hp- finite element methods: theory and applications in solid and fluid mechanics*, Oxford University Press, 1998.

- [38] I. Terrasse, *Résolution mathématique et numérique des équations de Maxwell instationnaires par une méthode de potentiels retardés*, Ph.D. thesis, École Polytechnique (1993).
- [39] H. Xiao, Z. Gimbutas, *A numerical algorithm for the construction of efficient quadrature rules in two and higher dimensions*, Computer and Mathematics with Applications, **59**, (2010), 663–676.
- [40] L. Xu, T. Kundu, *Stress singularities at crack corners*, Journal of Elasticity, **39**, (1995), 1–16.